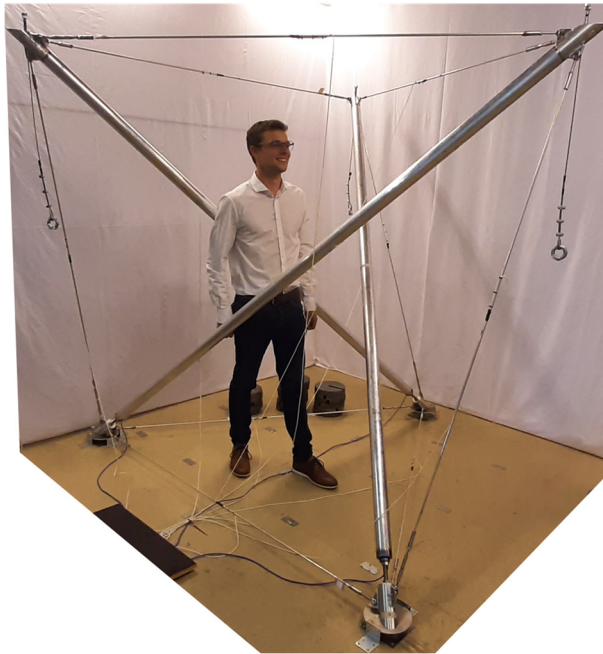


# Experimental testing of a tensegrity simplex: self-stress implementation and static loading

ASCE Journal of Structural Engineering

Self-stress



Loading



Jonas FERON, Landolf RHODE-BARBARIGOS, Pierre LATTEUR

## References of the article:

Feron J., Rhode-Barbarigos L., Latteur P., 2023, "Experimental testing of a tensegrity simplex: self-stress implementation and static loading", **Journal of Structural Engineering**, 149 (7)  
DOI: 10.1061/JSENDH.STENG-11517

**This is the Accepted version of the article. The published version is available online:**

<https://doi.org/10.1061/JSENDH.STENG-11517>

**Contact:** pierre.latteur@ucouvain.be, jonas.feron@besix.be

Thank you for your interest,  
The authors

# Experimental testing of a tensegrity simplex: self-stress implementation and static loading

Jonas FERON<sup>1</sup>, Landolf RHODE-BARBARIGOS<sup>2</sup>, Pierre LATTEUR<sup>3</sup>

<sup>1</sup> Ph.D. Candidate,

Université catholique de Louvain UCLouvain,

Institute of Mechanics, Materials and Civil Engineering IMMC,

Dept. of Civil and Environmental Engineering GCE,

Place du Levant, 1 (Vinci), bte L5.05.01, 1348-Louvain-la-Neuve, Belgium

jonas.feron@uclouvain.be;

BESIX,

Avenue des communautés, 100, 1200 Brussels, Belgium.

jonas.feron@besix.com

<sup>2</sup> Assistant Professor, University of Miami,

College of Engineering, Dept. of Civil & Architectural Engineering

1251 Memorial Drive, McArthur Engineering Bldg., Coral Gables, FL 33146, United States

landolfrb@miami.edu

<sup>3</sup> Professor, Université catholique de Louvain UCLouvain,

Institute of Mechanics, Materials and Civil Engineering IMMC,

Dept. of Civil and Environmental Engineering GCE,

Place du Levant, 1 (Vinci), bte L5.05.01, 1348-Louvain-la-Neuve, Belgium

pierre.latteur@uclouvain.be

27    **Abstract:**

28           A physical model of the simplest three-dimensional tensegrity unit was built at human-scale out of  
29    aluminum. Self-stress implementation and static loading tests were performed on this model. At each step,  
30    accurate measurements were obtained for all nodal positions and element forces. For the prestressing phase,  
31    elongations were imposed, via mechanical devices, in different combinations of elements, called prestress  
32    scenarios. Experimental results are compared to the theoretical self-stress state obtained by singular value  
33    decomposition of the equilibrium matrix and to numerical simulations using the dynamic relaxation method.  
34    It is shown that internal forces follow the same linear trend for all prestress scenarios even if the geometry is  
35    significantly impacted. Compressive tests were conducted by hanging masses from the top nodes. It is shown  
36    that there exists a unique load-displacement relation, that follows the “infinitesimal” mechanism direction for  
37    a “finite” distance which depends on the self-stress level. The paper provides a detailed overview of the  
38    simplex’s structural behavior using both experimental and numerical results while discussing the limitations  
39    of the analysis methods explored.

40    **Practical Applications:**

41           Tensegrity structures are composed of compressive elements floating inside a network of prestressed  
42   cables. Their unique esthetics and mechanical properties have always amazed architects, scientists, and  
43   engineers. However, the number of tensegrity structures built for civil purposes remains limited. Reasons  
44   behind this include a non-intuitive structural behavior with occurrences of insufficient stiffness and lack of  
45   robustness as well as a complex construction process which requires introduction of prestressing forces.  
46   Consequently, tensegrity structures are often distrusted in favor of other structural systems. Many studies have  
47   focused on finding the conditions required for the existence of self-equilibrated prestressing forces that  
48   provide stability and stiffness in tensegrity structures. However, few studies have focused on how these  
49   prestressing forces can be implemented in a structure, and the discrepancy between theoretical and numerical  
50   approaches. For these reasons, a full-scale physical model of a tensegrity module was built and tested with  
51   extreme care on the design and experimental testing. This paper presents a comparison of experimental results  
52   using two established analysis methods discussing the differences between experimental measurements and  
53   numerical models.

54  
55   **Keywords:** self-stress mode, infinitesimal mechanism, equilibrium matrix, dynamic relaxation, sensitivity  
56   matrix.

## 57 NOTATION LIST

58 The following symbols are used in this paper:

Notation	Unit	Description
$[ \quad ], \{ \quad \}$	varies	<b>[Matrices]</b> , <b>{Vectors}</b> use <b>bold font</b> but not the <i>scalars</i> .
$[A]$	[-]	Equilibrium matrix contains the element direction cosines in the current geometry of the structure. For the prestressing phase of this simplex, $[A]$ is computed in the theoretical geometry and assumed constant.
$[A]^T$	[-]	The compatibility matrix is the Transpose of the equilibrium matrix.
$A_c$	[mm <sup>2</sup> ]	Cross-sectionnal area of the cables (horizontal and vertical).
$A_i$	[mm <sup>2</sup> ]	Cross-sectionnal area of the element (strut or cable) $i$ .
$A_s$	[mm <sup>2</sup> ]	Cross-sectionnal area of the struts.
$\{a\}, a$	[N]	Vector of $s$ self-stress levels $\{a\}$ associated to $s$ self-stress modes $[S]$ . For this simplex, there is $s = 1$ scalar self-stress level $a$ .
$a_{gov}$	[N]	The simplex' maximum self-stress level is governed by the tensile strength of the vertical cables.
$\Delta a$	[N]	Variation of the simplex' self-stress level induced by the elongation imposed $\{\bar{e}\}$ .
$[C]$	[kg/s]	Damping matrix. In the dynamic relaxation algorithm, kinetic damping is used.
$\{d\}$	[mm]	Vector of nodes displacements in the free directions (i.e. not fixed by a support).
$E_i$	[MPa]	Equivalent Young's modulus of the element $i$ (that considers all parts composing the element).
$\{e\}$	[mm]	Vector of elastic length variation (elongation positive) induced by the axial force in each element.
$\{\bar{e}\}$	[mm]	Vector of imposed elongations by mechanical devices in each element, i.e. the prestress scenario.
$\{f\}$	[N]	Vector of external loads applied on the nodes in the free directions (i.e. not fixed by a support).
$f^m$	[N]	Orthogonal projection ( $=\{U^m\}^T\{f\}$ ) of the external loads on the simplex' mechanism.
$H_3, H_4, H_5$	[mm]	Height of the top nodes of the simplex. Index $i$ ( $=3, 4$ , or $5$ ) in $H_i$ relates to the index of the top node. $H$ is used when $H_3 = H_4 = H_5$ .
$[I]$	varies	Identity matrix.
$[K^e]$	[N/mm]	The element stiffness matrix is a diagonal matrix where each diagonal entry $K_{ii}^e$ is equal to the stiffness $E_i A_i / l_i$ of the element $i$ .
$[K^G]$	[N/mm]	Geometric stiffness matrix of the structure.
$[K^M]$	[N/mm]	Material stiffness matrix of the structure given by $[A][K^e][A]^T$ .
$[K^S], K^S$	[N/mm]	Stiffness matrix of the self-stress modes $[S]$ . For this simplex, the unique self-stress mode has a scalar stiffness $K^S$ .
$[K^T]$	[N/mm]	Tangent stiffness matrix of the structure given by $[K^M] + [K^G]$ .
$K^T$	[N/mm]	Tangent stiffness scalar (non constant) in the simplex' mechanism direction such that $f^m = K^T \beta$ .
$l_i$	[mm]	Free length of the element $i$ . Free lengths can be altered by imposed elongations $\{\bar{e}\}$ .
$[M]$	[kg]	Matrix of the nodal masses
$m$	[-]	Number of mechanisms or degree of kinematic indeterminacy.
$[SM^a]$	[N/mm]	Self-stress level(s) sensitivity matrix correlates linearly the imposed elongations with the self-stress levels.
$[SM^t]$	[N/mm]	Forces sensitivity matrix correlates linearly the imposed elongations with the elements forces.
$[SM^{d_i}]$	[mm/mm]	Three different formulations (depending if $i = 1, 2$ , or $3$ ) of the displacement sensitivity matrix that correlates linearly the imposed elongations with the nodes displacements.
$[S], \{S\}$	[-]	Matrix $[S]$ contains $s$ self-stress modes $\{S\}$ . In this simplex, there is $s = 1$ self-stress mode $\{S\}$ .
$s$	[-]	Number of self-stress modes or degree of static indeterminacy.
$\{t\}$	[N]	Vector of axial forces (tension positive) in the elements.
$[U^m], \{U^m\}$	[-]	Matrix $[U^m]$ contains $m$ inextensional displacements modes $\{U^m\}$ (i.e. mechanisms). In this simplex, there is $m = 1$ mechanism $\{U^m\}$ .
$\{\dot{v}\}, \{v\}$	[m/s <sup>2</sup> ], [m/s]	Acceleration, velocity of the nodes in the free directions
$\alpha_3, \alpha_4, \alpha_5$	[°]	Angles of rotation between the top and bottom triangular bases of the simplex. Index $i$ ( $=3, 4$ , or $5$ ) in $\alpha_i$ relates to the index of the top nodes. $\alpha$ is used when $\alpha_3 = \alpha_4 = \alpha_5$ .
$\{\beta\}, \beta$	[mm]	Vector of $m$ coefficients $\{\beta\}$ associated to the activation of the $m$ mechanisms $[U^m]$ . For this simplex, there is $m = 1$ mechanism activation scalar $\beta$ .

59     **INTRODUCTION**

60             Tensegrity structures are made of struts surrounded by prestressed cables. Their esthetics and  
61     performance have called the attention of the scientific community for seventy years across different  
62     disciplines. However practical applications are still rare (Micheletti & Podio-Guidugli, 2022). The present  
63     study aims at characterizing a physical model of the simplest tensegrity three-dimensional unit called simplex  
64     (or triplex) in an effort to provide an overview of its structural behavior during the implementation of self-  
65     stress and under static loading. The study compares conventional analysis methods with physical  
66     measurements and discusses the limitations of the selected methods.

67             Tensegrities are defined as “*systems in a stable self-equilibrated state comprising a discontinuous set*  
68     *of compressed components inside a continuum of tensioned components*” (Motro, 2003) but other definitions  
69     exist (Hanaor, 2012; Jauregui, 2010; Obara et al., 2019; Oliveira & Skelton, 2009). Prestress is vital for  
70     tensegrity structures in the same way that internal pressure is critical for air-supported (pneumatic) structures.  
71     Their geometry can thus only be defined if internal forces in the elements composing the structure are in self-  
72     equilibrated prestress state. Tensegrity structures often exhibit a geometrically non-linear load-displacement  
73     relation which may be attributed to the flexibility of their tensile elements (cables) and/or to the existence of  
74     internal mechanism(s). Tensegrity structures are thus statically indeterminate and may also be kinematically  
75     indeterminate systems (Calladine, 1978; Pellegrino, 1990, 1993; Pellegrino & Calladine, 1986).

76             Despite the interest on tensegrity structures by structural engineers, few civil tensegrity applications  
77     exist (Kawaguchi & Lu, 2002; Kawaguchi & Mizutani, 2018; Klimke & Stephan, 2004; Paronesso, 2002;  
78     Paronesso & Passera, 2004; Schlaich, 2004). Common barriers for their application include:

- 79             -     **Identifying an appropriate stable configuration** (Aloui et al., 2018a, 2019; Recski, 2008; J. Y.  
80                     Zhang & Ohsaki, 2007). This relates to defining a stable tensegrity system that satisfies the  
81                     project’s architectural and structural criteria and constraints (Feron et al., 2019, 2021; Hrazmi et

al., 2021; Micheletti, 2012; Rhode-Barbarigos et al., 2010). Designing a tensegrity structure starts with form finding i.e. the identification of the self-stress forces and the equilibrated geometry. There is variety of methods that can be explored for the form finding of tensegrity structures (Tibert & Pellegrino, 2003; Veenendaal & Block, 2012). It should be noted however that the use of the so-called force-density methods (FDM) (Schek, 1974; Vassart & Motro, 1999) may be cumbersome while trying to satisfy a project's constraints as the method typically provides no control over the lengths of the elements (Tibert & Pellegrino, 2003). On the opposite, dynamic relaxation methods (DRM) (Barnes, 1988, 1999; Day, 1965) seek for a geometry in equilibrium while imposing the elements free lengths.

- **Their complex mechanical behavior** (Bel Hadj Ali et al., 2011; Juan & Mirats Tur, 2008; Murakami, 2001). Once a stable tensegrity configuration has been defined through form finding, the structure is then analyzed and sized under load actions which may require iterative computational schemes (Faroughi & Lee, 2014; Kebiche et al., 1999; P. Zhang et al., 2014) or not (P. Zhang et al., 2020). Moreover, the behavior of tensegrity structures under loading as well as its stability are known to be affected by prestressing (Connelly, 2002; Deng & Kwan, 2005; Guest, 2011; Pellegrino, 1990; J. Y. Zhang & Ohsaki, 2007).

- **The complexity of their construction** (Kawaguchi & Mizutani, 2018; Klimke & Stephan, 2004). Eventually, the structure is erected by connecting the different elements together and by prestressing the system. A common challenge during the prestress introduction is shape control (Kawaguchi et al., 1996; Xu & Luo, 2009; You, 1997; Yuan et al., 2016) while also considering element-length tolerances and actual material behavior (Chen et al., 2016, 2020; Luo et al., 2016).

Although many studies have focused on the form finding and analysis of tensegrity structures using numerical methods (Estrada et al., 2006; Tibert & Pellegrino, 2003; Veenendaal & Block, 2012; Wang et al., 2021; P.

105 Zhang et al., 2014, 2020), few studies have addressed challenges related with the physical implementation of  
106 the concept. In practice, the targeted self-stress in a tensegrity structure is implemented by shortening or  
107 lengthening one or multiple cables and/or struts of the system. This is typically done using engineering  
108 judgement by arbitrary choosing a *prestress scenario*, i.e. a set of imposed elongations. The concept of  
109 sensitivity matrix (SM) allows to linearly correlate the increase of prestress forces as a function of the chosen  
110 prestress scenario (Kawaguchi et al., 1996; Kwan & Pellegrino, 1993; Xue et al., 2021). Note that one way to  
111 compute numerically the SM is to impose a unitary elongation in each element individually and to assess the  
112 resulting prestress forces in all elements. However, depending on the amplitude of the length variations and  
113 on the choice of elements being prestressed, the geometry and the distribution of the prestress forces may be  
114 impacted (Saeed, 2022; Xu & Luo, 2009; Yuan et al., 2016). As shown here below, no experimental study  
115 was found that investigates both the increase of prestress forces in the system and the displacements as a  
116 function of the imposed length variation:

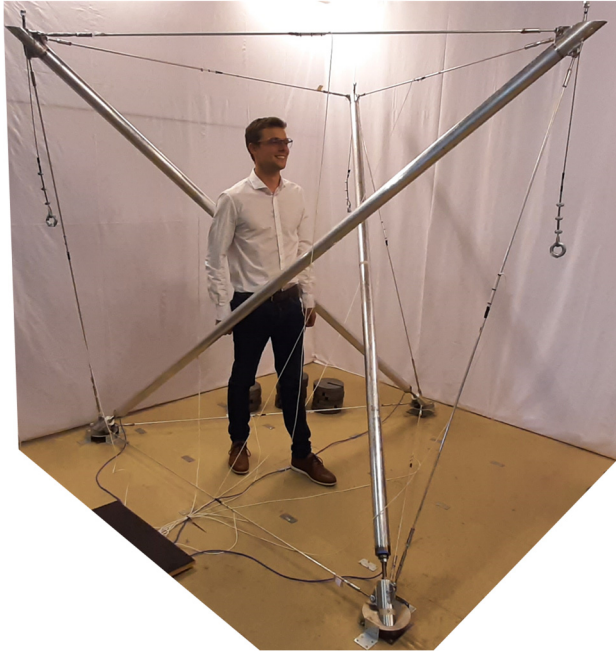
- 117 - Kawaguchi et al. (1996) measured the prestress forces of a  $6 \times 9.5 \times 2.3$  m tension stabilized truss  
118 resulting from the shortening of one cable. However, a linear response of the prestress forces and  
119 displacements was assumed as the amplitude of the shortening was relatively small.
- 120 - You (1997) measured the prestress forces and displacements by acting on four of the nine cables  
121 of a  $1.8 \times 0.72$  m two-dimensional cable net in order to control its shape. Measurements were taken  
122 for one amplitude of length variation with the response of the structure assumed to be linear.
- 123 - Early 2000s, the research team of the University of Montpellier II (Averseng et al., 2002; Averseng  
124 & Crosnier, 2004; Dubé et al., 2008) studied experimentally a  $3.2 \times 3.2 \times 0.8$  m square double-layer  
125 tensegrity grid and proposed a prestressing method for structures with multiple self-stress states  
126 (Averseng & Crosnier, 2004). However, the method assumes that the employed prestress scenario  
127 does not distort the geometry which is unknown a priori.



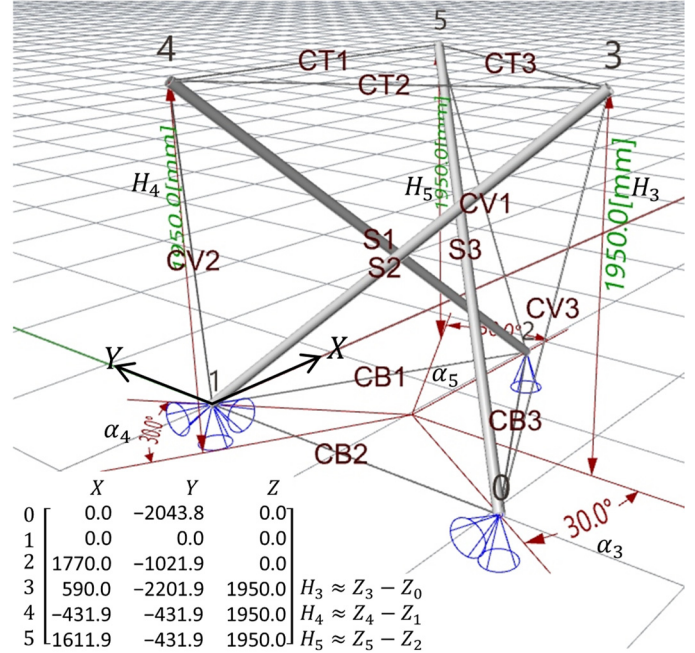
- More recently, Shekastehband, et al. (2013) tested a  $3 \times 3 \times 0.7$  m tensegrity grid and proposed a method for implementing self-stress in tensegrity structures for civil applications. The method requires the structure to be restrained by a secondary rigid system that maintains its shape throughout the process as well as a series of prestressing corrections after release.

Investigating the effects of self-stress implementation in tensegrity structures is critical for their application. This paper focuses on the introduction of self-stress in a free-standing tensegrity simplex model and its static behavior under vertical loading considering two different self-stress levels. The simplex model (Figure 1) was built and tested experimentally in the lab “Laboratoire d’Essais Mécaniques, Structures et genie Civil” (LEMSC) at the Catholic University of Louvain (UCLouvain) in Belgium. All nodal displacements and element forces were recorded during testing with all data publicly available in (Feron et al., 2022). Experimental results are compared to two established analysis methods: linear analyses based on the equilibrium matrix (*theoretical method*) and nonlinear analysis using dynamic relaxation (*numerical method*).

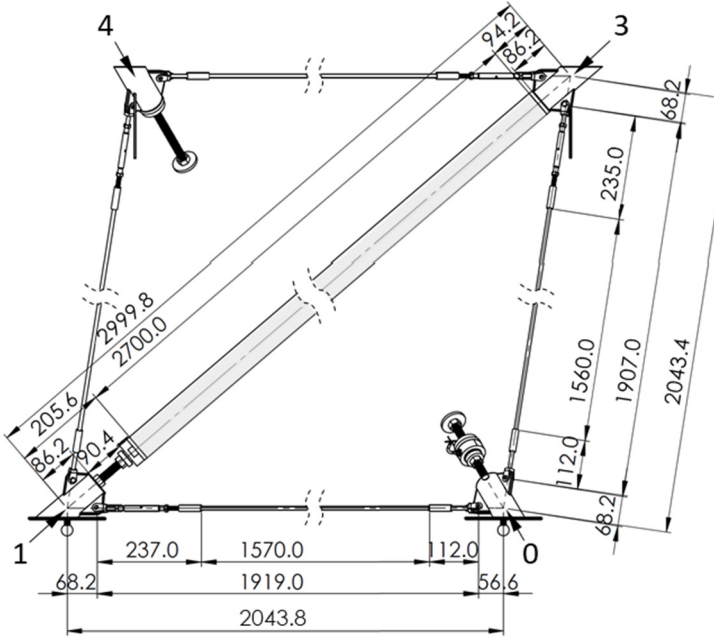
The paper is organized as follows; The *background* chapter describes the two analysis methods. The *material and methods* section describes the physical model of the simplex, its theoretical self-stress mode and infinitesimal mechanism as well as the experimental protocol for the testing. The *results* section presents the comparison of the experimental testing with the results of the theoretical and numerical analyses. Results focus on the internal forces distribution, nodal height and angle of rotation when considering different prestress scenarios and loading on the top nodes. The *discussion* section includes an analysis of the results, as well as a discussion on their validity and limitations. Finally, conclusions are summarized in the last (*conclusions*) section.



a



b



c

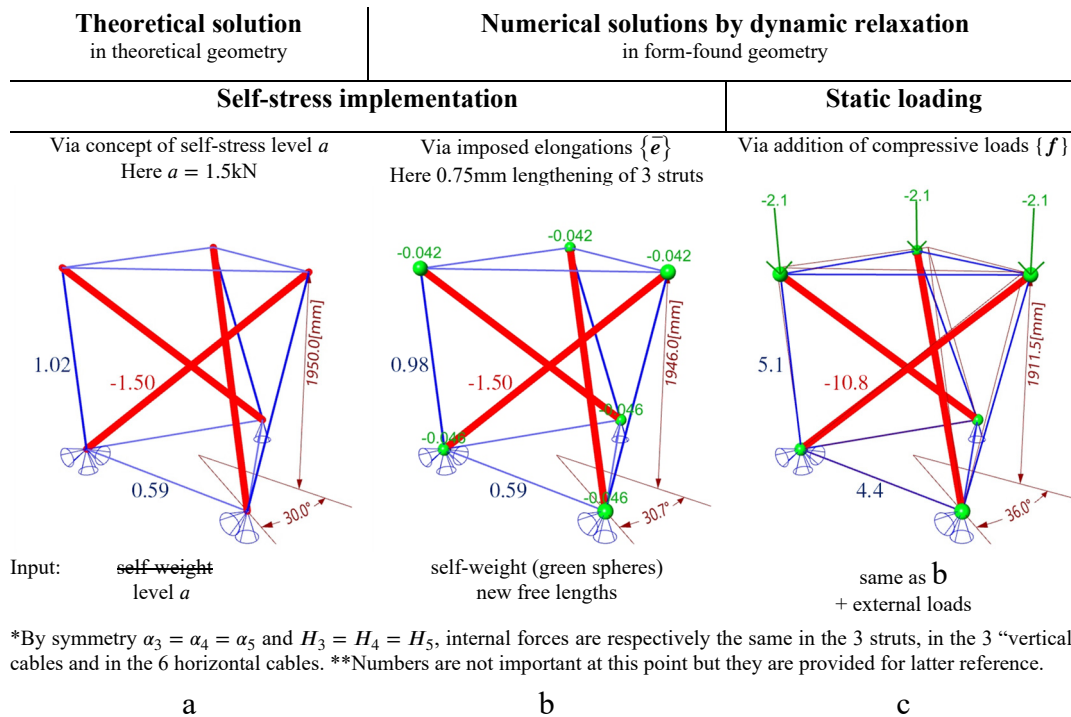


d

Figure 1. The simplex physical model (dimensions in mm). a: General perspective; b: Illustration of the model with node indexes and coordinates, and element denomination; c: Front view in the CAD model and lengths; d: Joint detail.

# 153 BACKGROUND

154 The goal of this paper is to provide a detailed view of the static behavior of the tensegrity simplex  
 155 through physical testing and a benchmark for future computational developments. Experimental results on the  
 156 simplex model are thus compared to the theoretical solution assuming no self-weight (Figure 2.a) and to  
 157 numerical solutions obtained using dynamic relaxation (Figure 2.b and c). The theoretical and numerical  
 158 methods selected are discussed below. The reader should note that other methods, such as analytic solutions  
 159 (Fraternali et al., 2015; Oliveira & Skelton, 2009, pp. 107–110) and displacement-based finite elements  
 160 methods (Faroughi & Lee, 2014; Kebiche et al., 1999; Ma et al., 2022; P. Zhang et al., 2014), are available  
 161 and could have been used in this comparison. A complete comparison and the improvement of existing  
 162 methods is however out of the scope of this paper. Experimental results are open-accessible (Feron et al.,  
 163 2022) for interested readers willing to explore other methods.



164 Figure 2. Theoretical and numerical solutions used for comparison with the physical model ([kN] unless otherwise specified), a: the theoretical  
 165 self-stress state without self-weight, b: the numerically form-found simplex with self-weight, c: simplex under external loading.

## 167 Theoretical method for self-stress evaluation

168 The form finding and the analysis of truss-like structures is ruled by equilibrium equations, material  
169 laws and compatibility equations (Pellegrino, 1990; Pellegrino & Calladine, 1986), respectively written as:

$$[A]\{t\} = \{f\} \quad (1)$$

$$\{e\} = [K^e]^{-1}\{t\} \quad (2)$$

$$[A]^T\{d\} = \{e\} + \{\bar{e}\} \quad (3)$$

170 where  $[A]$  and  $[A]^T$  are respectively the equilibrium matrix and its transpose also known as  
171 compatibility matrix.  $[K^e]$  is the element stiffness matrix assuming linear elastic materials (Hooke law),  $\{t\}$   
172 are the axial forces in the elements,  $\{f\}$  are the external loads,  $\{e\}$  are the elastic elongations of the elements,  
173  $\{\bar{e}\}$  are the imposed elements elongations by the mechanical devices, and  $\{d\}$  are the nodal displacements in  
174 the three directions.

175 At prestressing stage, the effects of the imposed elements elongations  $\{\bar{e}\}$  are studied in terms of  
176 internal force and displacement increases while external loads and self-weight are typically neglected ( $\{f\} =$   
177  $\{0\}$ ). Hence, substituting equation ( 2 ) into ( 3 ) leads to:

$$[A]^T\{d\} = [K^e]^{-1}\{t\} + \{\bar{e}\} \quad (4)$$

178 with equation ( 1 ) becoming in the absence of external loads:

$$[A]\{t\} = \{0\} \quad (5)$$

179 Imposed elements elongations  $\{\bar{e}\}$  may thus produce a non-trivial solution for internal forces  $\{t\} \neq$   
180  $\{0\}$ , i.e. a self-equilibrated state. Self-stress states  $\{t\}$  exist only in statically indeterminate structures  
181 (Calladine, 1978; Pellegrino & Calladine, 1986). For a degree  $s$  of static indeterminacy, the self-stress state  
182  $\{t\}$  is obtained by linear combination of the  $s$  self-stress modes  $[S]$  with their associated self-stress levels  $\{a\}$   
183 such that:

$$\{t\} = [S]\{a\} \quad (6)$$

184 The  $s$  independent self-stress modes  $[S]$  represent the null space of the equilibrium matrix  $[A]$  and can  
185 be obtained through its singular value decomposition (SVD) (Pellegrino, 1993).

Kwan and Pellegrino (1993) proved imposed elongations  $\{\bar{\mathbf{e}}\}$  and self-stress levels increase  $\{\mathbf{a}\}$  are linearly correlated according to the self-stress levels sensitivity matrix  $[\mathbf{SM}^a]$  :

$$\{\mathbf{a}\} = \underbrace{-([\mathbf{S}]^T[\mathbf{K}^e]^{-1}[\mathbf{S}])^{-1}[\mathbf{S}]^T}_{[\mathbf{SM}^a]} \{\bar{\mathbf{e}}\} \quad (7)$$

Whereas the internal force increase is obtained via the forces sensitivity matrix  $[\mathbf{SM}^t]$  by back substitution of equation ( 7 ) into ( 6 ):

$$\{\mathbf{t}\} = \underbrace{[\mathbf{S}][\mathbf{SM}^a]}_{[\mathbf{SM}^t]} \{\bar{\mathbf{e}}\} \quad (8)$$

Substituting equation ( 8 ) into ( 4 ) leads to:

$$[\mathbf{A}]^T\{\mathbf{d}\} = ([\mathbf{K}^e]^{-1}[\mathbf{SM}^t] + [\mathbf{I}])\{\bar{\mathbf{e}}\} \quad (9)$$

The nodal displacements induced by imposed elongations can eventually be obtained (Kawaguchi et al., 1996; You, 1997) by introducing the concepts of pseudo-inverse  $[\mathbf{A}]^{T+}$  and null space  $[\mathbf{U}^m]$  of the compatibility matrix such that:

$$\{\mathbf{d}\} = [\mathbf{A}]^{T+}([\mathbf{K}^e]^{-1}[\mathbf{SM}^t] + [\mathbf{I}])\{\bar{\mathbf{e}}\} + [\mathbf{U}^m]\{\boldsymbol{\beta}\} \quad (10)$$

Displacements can be traced to three sources. The ones produced from *elastic* elongations  $\{\mathbf{e}\}$  or from *imposed* elongations  $\{\bar{\mathbf{e}}\}$  are called *extensional* displacements while the ones produced, in kinematically indeterminate structures of degree  $m$ , by the activations  $\{\boldsymbol{\beta}\}$  of the  $m$  *mechanisms*  $[\mathbf{U}^m]$  are called *inextensional* displacements. The  $m$  independent mechanisms  $[\mathbf{U}^m]$  (Calladine & Pellegrino, 1991) are usually computed also through SVD of the equilibrium matrix (Pellegrino, 1993). It is typically assumed that “in practical kinematically indeterminate structures, the inextensional displacements modes are restricted through prestressing” (Xue et al., 2021), hence the coefficients  $\{\boldsymbol{\beta}\}$  associated to the activation of the mechanisms  $[\mathbf{U}^m]$  are null. The displacements can thus be expressed as a function of the displacements sensitivity matrix  $[\mathbf{SM}^{d1}]$ :

$$\{\mathbf{d}\} = \underbrace{[\mathbf{A}]^{T+}([\mathbf{K}^e]^{-1}[\mathbf{SM}^t] + [\mathbf{I}])}_{[\mathbf{SM}^{d1}]} \{\bar{\mathbf{e}}\} \quad (11)$$

Xue et al. (2021) demonstrated that the displacements sensitivity matrix  $[SM^{d1}]$  could also be expressed as  $[SM^{d2}]$ :

$$[SM^{d2}] = [K^M]^+ [A][K^e] \quad (12)$$

Where  $[A][K^e]$  is the linear mapping transforming the imposed elongations  $\{\bar{e}\}$  into equivalent external loads  $\{f\}$  and  $[K^M]^+$  is the pseudo-inverse of the structure material stiffness matrix  $[K^M] = [A][K^e][A]^T$ . They conclude that the displacements sensitivity matrix shall consider the influence of the geometrical stiffness  $[K^G]$  and suggest using the tangent stiffness matrix  $[K^T] = [K^M] + [K^G]$  in the formulation of  $[SM^{d3}]$  as follows:

$$[SM^{d3}] = [K^T]^{-1} [A][K^e] \quad (13)$$

Although displacements can be calculated using theoretical approaches, the geometry is typically assumed constant without any distortion during prestressing. This assumption implies that the equilibrium matrix  $[A]$  and its associated self-stress modes  $[S]$  computed on the basis of the initial geometry remain valid for all amplitudes of imposed length variations (Saeed & Kwan, 2016; Xue et al., 2021; P. Zhang et al., 2020). Few numerical approaches were found to consider the geometric distortions through iterative schemes (Saeed, 2022; Xu & Luo, 2009; Yuan et al., 2016; P. Zhang et al., 2014). Nevertheless, no experimental evidence was found to support the consistency of both approaches. Hence, the present study assumes no geometric distortion while prestressing (see Figure 2.a) which will be later discussed.

## Numerical method for self-stress evaluation and loading

The numerical method explored in this paper is dynamic relaxation (Day, 1965). While the theoretical method assumed no self-weight, the numerical method takes it into account in the self-stress evaluation (Figure 2.b). The numerical method is also used to estimate displacement and forces of the physical model under external loads (Figure 2.c). When loads are applied on the structure, new nodes coordinates are sought where the internal forces are in equilibrium with the loads. Dynamic relaxation (DR) (Day, 1965) is a well-known form-finding and analysis method for tensile structures (Barnes, 1988, 1999) including tensegrity

structures (Bel Hadj Ali et al., 2011; Juan & Mirats Tur, 2008; Tibert & Pellegrino, 2003). The method transforms the static equilibrium problem into a pseudo-dynamic one with the solution obtained by tracing the motion of the nodes until the structure comes to rest in a stable static equilibrium due to damping. The governing equation for dynamic relaxation is:

$$\{\mathbf{f}\} - [\mathbf{A}]\{\mathbf{t}\} = [\mathbf{M}]\{\dot{\mathbf{v}}\} + [\mathbf{C}]\{\mathbf{v}\} \quad (14)$$

with  $\{\mathbf{f}\} - [\mathbf{A}]\{\mathbf{t}\}$  are the residual loads (i.e. the external loads that are not equilibrated with the internal forces in the current deformed geometry) evaluated at each node, while  $\{\dot{\mathbf{v}}\}$  and  $\{\mathbf{v}\}$  are the acceleration and the velocity at each node.  $[\mathbf{M}]$  corresponds to the nodal masses and  $[\mathbf{C}]$  corresponds to damping which, in this case, are fictitious. Masses and damping indeed do not need to represent the physical characteristics of the actual system because the focus is on finding the static solution with  $\{\dot{\mathbf{v}}\} = \{\mathbf{0}\}$  and  $\{\mathbf{v}\} = \{\mathbf{0}\}$ . Therefore, they can be optimized for the stability and convergence of the method (Belytschko & Hugues, 1983; Cundall, 1976; Papadrakakis, 1981). In this study, kinetic damping is used for convergence to the static equilibrium state (Barnes, 1999) with the motion of the structure traced throughout time. A detailed description of the dynamic relaxation algorithm explored in this paper can be found in (Bel Hadj Ali et al., 2011). The algorithm was re-implemented in Python and a Grasshopper-Rhino plug-in was developed as user interface for parametric structural analysis. Variables (free lengths and loads) can be easily modified while visual feedback is received on the equilibrium results (internal forces and nodes coordinates) at prestressing (Figure 2.b) and at loading stages (Figure 2.c).

## 243 MATERIALS AND METHODS

244 This section describes the physical model presenting its theoretical features (e.g. self-stress and  
245 inextensional displacements modes) followed by a description of the experimental method for testing.

### 246 Physical model

247 A human-scale physical model of a tensegrity simplex was designed and built for this study (Figure  
248 1.a). The simplex is a basic spatial tensegrity module with six nodes, nine elements in tension, and three  
249 elements in compression. Its equilibrium configuration can be obtained through form finding starting from a  
250 straight triangular prism and is described by a 30° relative rotation of its triangular bases (see Appendix A in  
251 (Feron et al., 2022)) or through the adhesion of two tensegrity cells that share four nodes and their fusion with  
252 the removal of two edges (Aloui et al., 2018b, 2019). The simplex has been studied extensively in literature  
253 (Feron et al., 2019; Fraternali et al., 2015; Motro et al., 1987; Roth & McCarthy, 2021; Sultan, 2014) often  
254 serving as paradigm for tensegrity investigations making it an ideal benchmark for this work.

#### 255 General description

256 The simplex geometry of the physical model is defined by three parameters: a height of 1950 mm, a  
257 circumscribed circle diameter of 2360 mm for its equilateral triangular bases, and an angle of rotation  $\alpha$  of  
258 30° between the two bases. This theoretical geometry serves as reference for the design and construction of  
259 the model. Figure 1.b illustrates the simplex geometry providing the nodal coordinates and the denomination  
260 of the elements. The model includes three struts (S1, S2, S3), three “vertical” cables (CV1, CV2, CV3), and  
261 six horizontal cables that can be distinguished between bottom cables (CB1, CB2, CB3) and top cables (CT1,  
262 CT2, CT3). The Young’s modulus, the areas and the lengths of all elements are summarized in Table 1 and  
263 discussed below.

264



Table 1. Summary of the element mechanical properties used in the theoretical and numerical methods

Elements	Index $i$ [-]	Young's Modulus $E_i$ [MPa]	Area $A_i$ [mm <sup>2</sup> ]	Length $l_i$ [mm]	Stiffness $K_{ii}^e = E_i A_i / l_i$ [N/mm]
S1, S2, S3	0-2	70390	364.4	2999.8	8551
CB1, CB2, CB3 CT1, CT2, CT3	3-8	71750	50.3	2043.8	1765
CV1, CV2, CV3	9-11	72190	50.3	2043.4	1776

### **Struts description**

Struts are made of aluminum EN-AW-6060-ET-T66 (CEN, 2009) tubes with an external diameter  $\phi_s = 60$  mm, an internal diameter 56 mm, a cross-sectional area  $A_s = 364.4$  mm<sup>2</sup> and a bending inertia  $I_s = 153,423$  mm<sup>4</sup>. It should be noted that the targeted theoretical strut length of 2999.8 mm is obtained through the combination of three parts (Figure 1.c): a 94.2 mm *upper end*, the 2700.0 mm *tube*, and a 205.6 mm *lower end*. The lower and upper ends of the struts are constituted of parts in aluminum and other parts (tube cups, threaded rods, etc.) made of stainless steel. The lower end of the struts includes an M16 threaded rod. Adjusting the length of the threaded rod between the tube and the cup allows correcting any differences observed in tube lengths as well as regulating prestress during testing (see Appendix B in (Feron et al., 2022)). The equivalent Young's modulus for the struts composed of the aluminum tubes and all other parts was estimated at 70.39 GPa (see Appendix C in (Feron et al., 2022)). The buckling resistance for the tubes is - 10.66 kN according to Eurocode (CEN, 2009) (see Appendix C in (Feron et al., 2022)). A single strut specimen was axially loaded (see Appendix C in (Feron et al., 2022)). This test allowed assuming that struts are perfectly straight with a bifurcation buckling behavior (no bending before the critical load).

### **Cables description**

Cables are made of aluminum EN-AW-6060-ER-T66 (CEN, 2009) rods with a diameter  $\phi_c = 8.0$  mm, a cross-sectional area  $A_c = 50.3$  mm<sup>2</sup> and a bending inertia  $I_c = 201$  mm<sup>4</sup>. Similar to the struts, the targeted theoretical cable length is obtained through a composition of a series of parts (Figure 1.c). For the 2043.8 mm

285 long horizontal cables, this includes a 68.2 mm joint attachment at one end, a 237.0 mm long steel *turnbuckle*,  
286 a 1570.0 mm long aluminum *rod*, a 112.0 mm long *passive end* and a 56.6 mm long joint attachment at the  
287 other end. The 2043.4 mm long “vertical” cables follow a similar configuration except that both lengths inside  
288 the joints are 68.2 mm, the turnbuckle is 235.0 mm long with the rod being 1560.0 mm long. Turnbuckles are  
289 employed to correct any differences observed in the cable lengths (from pin to pin disregarding the joint  
290 attachment) and regulate prestress during testing (see Appendix C in (Feron et al., 2022)). The Young’s  
291 modulus of both the horizontal and the “vertical” cables, composed of the aluminum rods and all other parts,  
292 is estimated at 71.75 GPa and 72.19 GPa, respectively (see Appendix C in (Feron et al., 2022)).

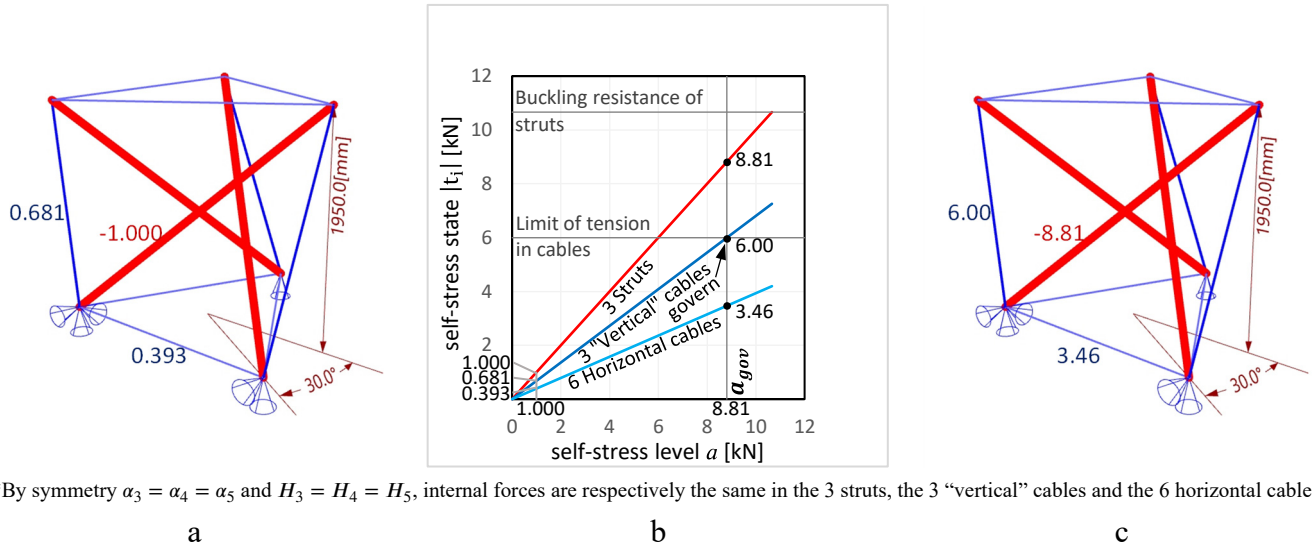
### 293 **Joints description**

294 Joints were designed to ensure that all elements of the tensegrity simplex are concurrent while  
295 maintaining element connectivity during testing. They were fabricated by welding three gusset plates on a  
296 truncated cylinder (Figure 1.d). The gusset-cylinder connection was made using a tenon-mortise joint to  
297 ensure the proper orientation of the elements according to the theoretical simplex geometry (see Appendix C  
298 in (Feron et al., 2022)). Bottom joints were attached to a circular plate and a ball allowing relative rotations  
299 of the supports while preventing rigid body motions of the model through the restriction of six degrees of  
300 freedom (see supports in Figure 1.b). The bottom joints restrict displacements in the vertical direction (Z axis).  
301 Joint 0 restricts also translation along the X axis only; the joint is resting on a rail oriented along the Y axis  
302 (Figure 1.a). Joint 1 is fixed in both X and Y directions, while Joint 2 is free to translate in the X-Y plane.

### 303 **Application of the theoretical method to the simplex model**

304 The tensegrity simplex is known (Connelly, 2002; Pellegrino, 1990) to be statically and kinematically  
305 indeterminate of degrees  $s = 1$  and  $m = 1$  even if the structure possesses twelve elements and twelve degrees  
306 of freedom (= three directions times six nodes minus six supports) (Calladine, 1978; Maxwell, 1864). The  
307 simplex has thus one self-stress mode  $\{S\}$  (see Figure 3.a) associated to a scalar self-stress level  $\alpha$  and one

mechanism  $\{\mathbf{U}^m\}$  associated to a scalar coefficient  $\beta$  (Figure 4). Both the self-stress mode and the mechanism can be obtained by SVD of the equilibrium matrix (Pellegrino, 1993) considering the theoretical geometry ( $H = 1950 \text{ mm}$ ,  $\alpha = 30.0^\circ$ ). Note that the self-stress mode  $\{\mathbf{S}\}$  and the mechanism  $\{\mathbf{U}^m\}$  have been rescaled in this paper (compared to SVD result). For instance, the mechanism  $\{\mathbf{U}^m\}$  was rescaled such that its activation by  $\beta = 10 \text{ mm}$  corresponds to vertical displacements of  $-10 \text{ mm}$  (Figure 4.b) and to rotation angles increase of  $1.6^\circ$  (Figure 4.c).



\*By symmetry  $\alpha_3 = \alpha_4 = \alpha_5$  and  $H_3 = H_4 = H_5$ , internal forces are respectively the same in the 3 struts, the 3 "vertical" cables and the 6 horizontal cables.

Figure 3. The simplex, a: self-stress mode  $\{\mathbf{S}\}$ [-], b: the self-stress state  $\{\mathbf{t}\}$ [kN] is a linear function of the scalar self-stress level  $a$ [kN] given the slopes  $\{\mathbf{S}\}$ , c: governing self-stress level  $a_{gov}$  [kN].

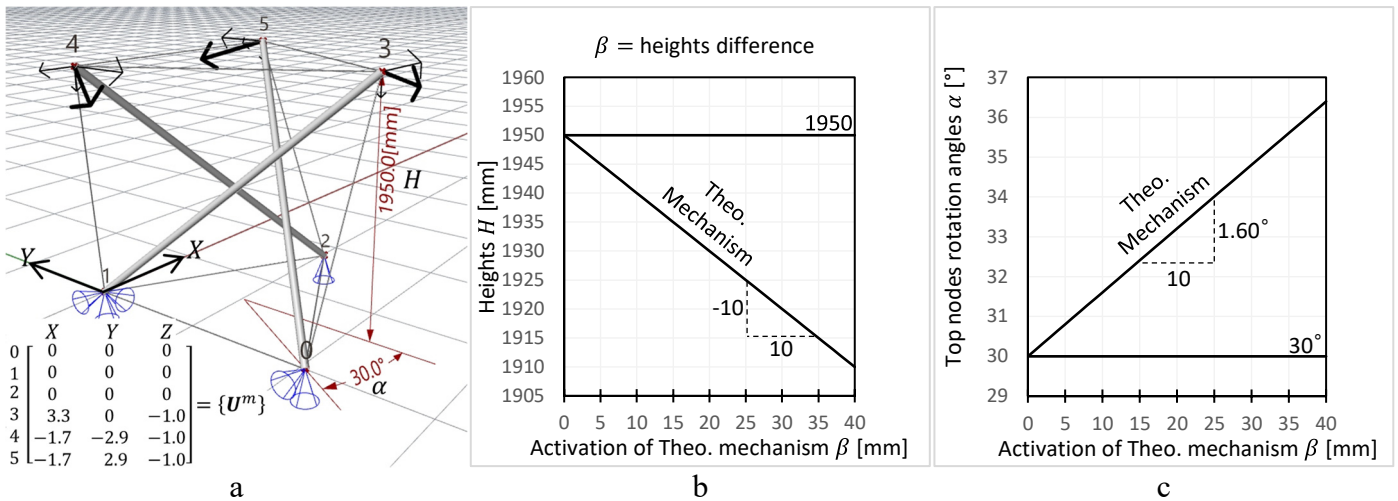


Figure 4. The twisting infinitesimal mechanism of the simplex, a: displacements  $\{\mathbf{d}\} = \{\mathbf{U}^m\}\beta$  [mm] due to unit activation  $\beta=1$ [mm] of the inextensional mode  $\{\mathbf{U}^m\}$ [-], b: Height  $H$  [mm] and c: Rotation angles  $\alpha$  [°] in function of the scalar coefficient  $\beta$ [mm].

Similarly, the self-stress level  $a = 1$  kN corresponds to the compression forces  $-1$  kN in the three struts (Figure 3.b). Therefore, at prestressing stage, the internal forces in all elements can be entirely defined by a single scalar  $a$  in kN such that  $\{t\} = \{S\}a$  (Figure 3.b). Considering the buckling resistance of  $-10.66$  kN for the struts and the tension limit of 6 kN in horizontal and vertical cables, a maximum self-stress level  $a_{gov}$  was defined (Figure 3.c). For this simplex model, the maximum self-stress level  $a_{gov} = 6/0.681 = 8.81$  kN is governed by the tension limit in the vertical cables with 0.681 representing the coefficient associated to the “vertical” cables in the self-stress mode (Figure 3.b).

It should be noted that the existence of a single self-stress mode  $\{S\}$  implies that prestressing one or multiple elements by imposed elongations  $\{\bar{e}\}$  should always result into forces that follow this distribution  $\{t\} = \{S\}a$  with increase in self-stress level  $a = [SM^a]\{\bar{e}\}$  obtained via the self-stress level sensitivity matrix  $[SM^a]$  with  $s = 1$  row (Table 2). Hence, lengthening one strut of the model by 1mm increases the self-stress level in the structure by 0.60 kN whereas shortening one horizontal cable or one vertical cable by 1 mm increases the self-stress level by 0.24 kN and 0.41 kN, respectively. Therefore, an error of  $\pm 1$ mm in the length of only one vertical cable will result in a self-stress level error  $a = \pm 0.41$  kN which is equivalent to force error ( $\{t\} = \{S\}a$ ) of  $\pm 0.41$  kN in struts,  $\pm 0.16$  kN in horizontal cables and  $\pm 0.28$  kN in vertical cables. It is thus clear that precision in element length measurements is important.

Table 2. Self-stress mode (vector) and self-stress level sensitivity matrix (of one row) of this simplex model

Elements	Index $i$ [-]	Self-stress mode $\{S\}$ [-]	Self-stress level sensitivity matrix $[SM^a]$ [N/mm]
S1, S2, S3	0-2	-1.000	+602
CB1, CB2, CB3 CT1, CT2, CT3	3-8	0.393	-237
CV1, CV2, CV3	9-11	0.681	-410

### **Loads description**

The self-weight of the structure including the weight of the elements with their respective parts as well as the weight of the joints themselves results in a load of 45.7 N and 41.6 N on bottom and top nodes,

339 respectively (Figure 2.b). Additional loads were applied to the top joints of the model during load testing.  
340 Masses of 10 kg were stacked on a 1.45 kg loading plate that was attached to a rope passing through the joints  
341 center. At maximum, the additional loads resulted in 2084 N/top node (Figure 2.c).

### 342 **Measurements description**

343 The response of the model to prestress variations and load application was monitored through load  
344 cells and strain gauges while changes in its geometry were obtained through optical measurements. Each strut  
345 was equipped with a Sensy load cell (Sensy, a) with precision  $\pm 0.025\text{kN}$  that measures the compressive force  
346 in it. Load cells were centered on the threaded rods M16 and were compressed between a 10mm thick loading  
347 washer (Sensy, b) and the stainless steel end cup of the tube. Compressive stresses can thus be assumed  
348 uniformly distributed on the sensor. Strain gauges were used to measure the tension in the cables. They were  
349 adhered on the lower side of the aluminum rods at mid length and calibrated through individual tensile tests  
350 of the cables in an MTS100kN (see Appendix C in (Feron et al., 2022)).

351 The geometry of the model was monitored using optical measurements. Each joint had a fixed marker  
352 that was tracked during testing using a *theodolite* Leica TPS1200+ series (Leica Geosystem). The optical  
353 system allowed tracking of the nodal coordinates with precision of  $\pm 1\text{mm}$  in space. This precision is  
354 reasonably good for nodal positioning and displacement computation. However, it cannot be used to calculate  
355 element lengths as precision would vary approximately by  $\pm 3.5\text{mm}$  ( $\pm \sqrt{3}\text{mm}$  at each element end). Elements  
356 lengths were thus computed based on tape measurements with a precision of  $\pm 0.5\text{mm}$  combined with a digital  
357 caliper (precision of  $\pm 0.01\text{mm}$ ) following (Averseng et al., 2002; Averseng & Crosnier, 2004).

358 For each experiment, all internal forces and displacements of the model were recorded throughout  
359 time. Experimental data are publicly available in (Feron et al., 2022).

## 360    **Experimental method**

361            The experimental testing focused first on the implementation of self-stress in the simplex model and  
362 then on the behavior of the structure under vertical loading considering two different self-stressed states.

### 363            **Starting points for the experiments**

364            All experimental testing (except the loading from high self-stress level) started from the form found  
365 configuration shown in Figure 2.b (including self-weight) with 1.5 kN in all the struts, 0.98 kN in all “vertical”  
366 cables and 0.59 kN in all horizontal cables. This initial state was chosen to ensure sufficient tension in the  
367 horizontal cables in order to neglect the bending/catenary effects due to self-weight (see Appendix C in (Feron  
368 et al., 2022)). All cables are thus assumed to be perfectly straight with a linear elastic behavior and bending  
369 strains in strain gauges measurements are negligible. In practice, the initial state is obtained before each test  
370 by adjusting the measured forces in the struts to 1.5 kN via struts lengths variations. At this initial state, all  
371 strain gauges are initialized at zero. Hence initial tensions in all cables are unknown but they are obtained by  
372 equilibrium using the measured compressive forces in the struts and the measured geometry of the model.  
373 Eventually, the combination of load cells in struts and strain gauges on the cables allows the characterization  
374 of the effects of prestress or external loading of the model.

375

### Self-stress implementation tests

For the prestressing phase, the prestress forces in the physical model were increased by imposing elongations  $\{\bar{\mathbf{e}}\}$  to selected elements. This paper discusses the results for different scenarios that consist in prestressing a) one horizontal top cable, b) one vertical cable, c) one strut, d) all three horizontal top cables, e) all three vertical cables, f) all three struts and g) all cables and struts. All prestressing experiments started from the same initial state shown in Figure 2.b which corresponds to a theoretical self-stress level with  $a = 1.5\text{kN}$  (Figure 2.a).

Moreover, prestress scenario g) which includes all cables and struts is referred here-after as a self-stress scenario. A *self-stress scenario* is here defined as a particular combination of imposed elongations  $\{\bar{\mathbf{e}}\}$  which results into a zero total elongation ( $\{\bar{\mathbf{e}}\} + \{\mathbf{e}\} = \{\mathbf{0}\}$ ) maintaining the theoretical geometry of the system. The imposed elongations  $\{\bar{\mathbf{e}}\}$  are thus such that they counterbalance the elastic strains  $\{\mathbf{e}\}$  caused by the prestress forces. Given equations ( 2 ) and ( 6 ), a self-stress scenario can be described as:

$$\{\bar{\mathbf{e}}\} = [\mathbf{K}^e]^{-1}[\mathbf{S}]\{\Delta\mathbf{a}\} \quad (15)$$

Table 3 shows the self-stress scenario obtained for the simplex model considering the physical properties of its elements (Table 1) and its self-stress mode (Table 2).

Table 3. Imposed elongations  $\{\bar{\mathbf{e}}\}$  in [mm] that lead to a self-stress scenario i.e. maintain the theoretical geometry of the system.

Elements	Self-stress level Increment	Self-stress scenario (see Figure 5.g)				
	$\Delta a = 1 \text{ [kN]}$	$a = 1.5 \text{ [kN]}$	$a = 3.2 \text{ [kN]}$	$a = 4.9 \text{ [kN]}$	$a = 6.6 \text{ [kN]}$	$a = 8.3 \text{ [kN]}$
S1, S2, S3	+0.117	+0	+0.20	+0.40	+0.60	+0.80
CB1, CB2, CB3	-0.223	-0	-0.38	-0.76	-1.14	-1.53
CT1, CT2, CT3	-0.384	-0	-0.66	-1.31	-1.97	-2.62

For each prestressing test, experimental results are compared to the theoretical and numerical self-stress evaluations with the imposed elongations  $\{\bar{\mathbf{e}}\}$  expressed as an increase of the theoretical self-stress level  $a$  (Figure 3.b) through the concept of the sensitivity matrix  $[\mathbf{SM}^a]$  (Table 2).

### **Static loading tests**

For load tests, masses of 10 kg per step were added to the top nodes of the model (see (Feron et al., 2022) for details on the loading scheme) starting from two different self-stress states. Both self-stress states were obtained by elongation of the three struts. The first experiment started thus from a theoretical self-stress level with  $a = 1.5$  kN (Figure 2.b) adding 2.1 kN on each top nodes (Figure 2.c), while the second experiment started from a self-stress level of  $a = 8.5$  kN adding 0.80kN on each top nodes. The maximum amount of load considered on the top nodes was dictated by element strength with the test starting with less prestress having more reserve for the loads. Loading experimental results are compared only to numerical results obtained using the dynamic relaxation method.

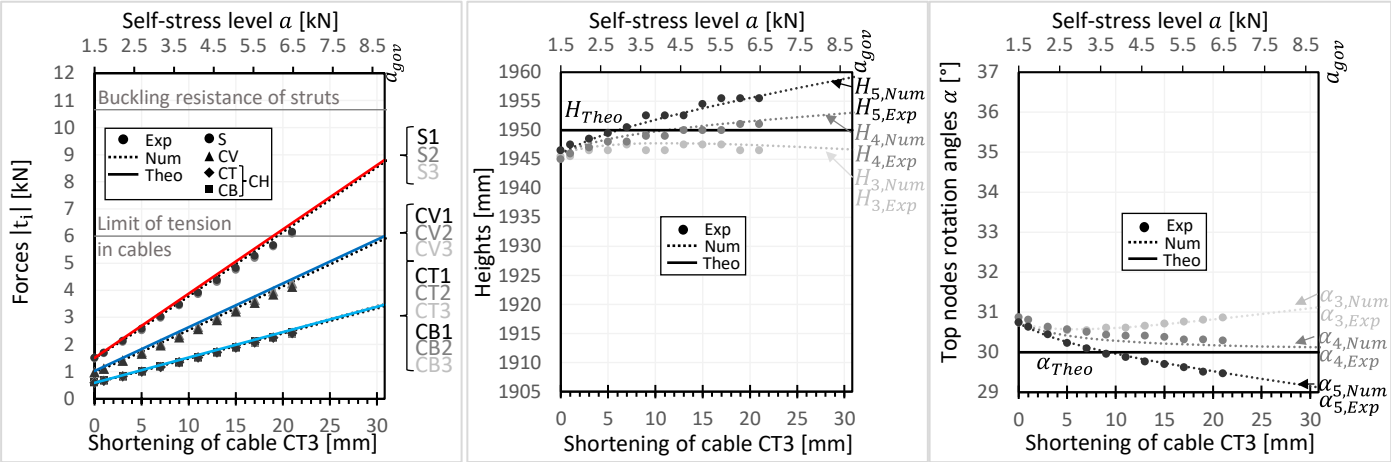


## 405    **RESULTS**

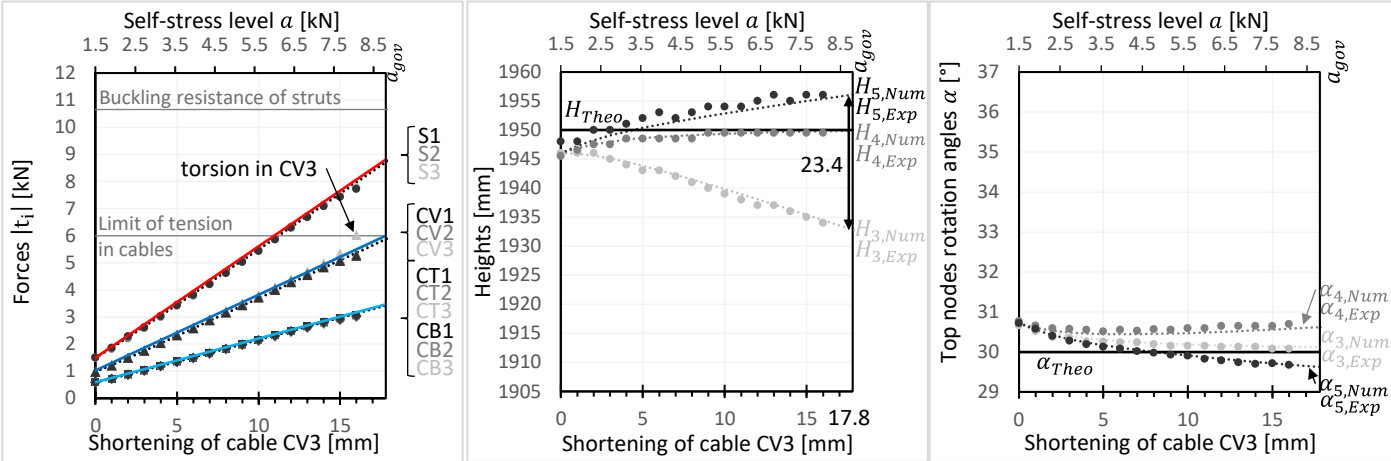
406            Figure 5 shows the effect of prestressing a) one horizontal top cable, b) one vertical cable, c) one strut,  
407    d) all three horizontal top cables, e) all three vertical cables, f) all three struts and g) all cables and struts in  
408    the internal forces of the model (first column) and its geometry (columns two and three). Given that the  
409    simplex model has a single self-stress mode, the internal forces in the model follow the same linear trend for  
410    all prestressing tests with only difference being the elongation imposed. Furthermore, prestressing tests  
411    correlate well in terms of forces with the theoretical self-stress state and the numerical simulations. The error  
412    between numerical and experimental results lies between 0 and 5% for all elements and all tests. Moreover,  
413    the theoretical self-stress state coincides almost perfectly with the numerical results obtained using dynamic  
414    relaxation which shows that self-weight has a negligible influence on the prestress forces. The self-stress state  
415    of the simplex (Figure 3.b) obtained through SVD of the equilibrium matrix based on the theoretical geometry  
416    remains thus valid for all prestressing tests.

417            Although forces follow the same trend, prestressing tests conducted by imposing elongations at  
418    different elements show notable differences in the geometry of the model (second and third columns of Figure  
419    5) revealing that the self-stress state can exist in multiple geometrical forms including asymmetrical ones. The  
420    measured heights and rotations are in agreement with the numerical results obtained using dynamic relaxation  
421    but deviate in some cases significantly from the theoretical geometry (Figure 1.b). Only the self-stress scenario  
422    (Figure 5.g) allows to obtain the theoretical geometry and that occurs for a relatively high self-stress level  
423    (when displacements due to self-weight become insignificant due to the stiffening effect of the self-stress on  
424    the mechanism). However, the implementation of the self-stress scenario may not be practical because it  
425    requires lengths variation and thus mechanical devices in all elements. If maintaining a symmetrical geometry  
426    is of interest, one can opt for a simpler prestress scenario with lengths variation in three elements only (see  
427    Figure 5 tests d, e, and f). The prestressing of three elements of the same group results in the targeted self-

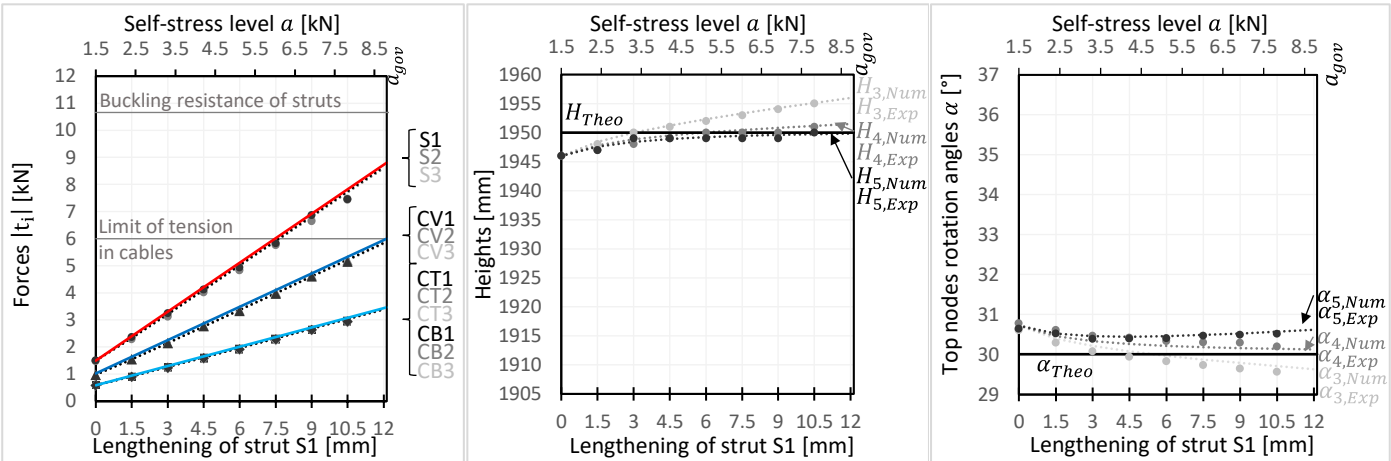
428 stress state while maintaining a horizontal top surface with angles  $\alpha_3$ ,  $\alpha_4$  and  $\alpha_5$  trending towards  $30^\circ$ .  
429 However, this prestressing implementation does not preserve the theoretical height of 1950.0mm with  
430 differences from -3.8mm (three vertical cables) to +3.1mm (three top cables) at maximum self-stress level  
431  $\sigma_{gov}$ . It should be noted that the targeted self-stress can always be obtained by actuating one element only (see  
432 Figure 5 tests a, b and c) but in these cases the geometry can be significantly distorted. For instance, an  
433 17.8mm shortening in one vertical cable will result in a 23.4mm height difference of the top base (Figure 5.b).  
434 Figure 5.b also shows torsion in cable CV3 which was being shortened by a turnbuckle. The torsion  
435 strains added up to the tension strains measured by the strain gauge of CV3 resulting in an higher apparent  
436 tension force. The torsion strains were generated in cable CV3 because, under almost 6kN of tension, the  
437 friction in the threads was preventing the turnbuckle from further shortening. It must be reminded that the  
438 failure of metals subjected to torsion can be brittle and must be prevented. To avoid such effects from torsion,  
439 highest tension was limited to 4.5kN in the prestressing of the three vertical cables (Figure 5.e) and vertical  
440 cables were shortened first in the self-stress scenario (Figure 5.g).  
441



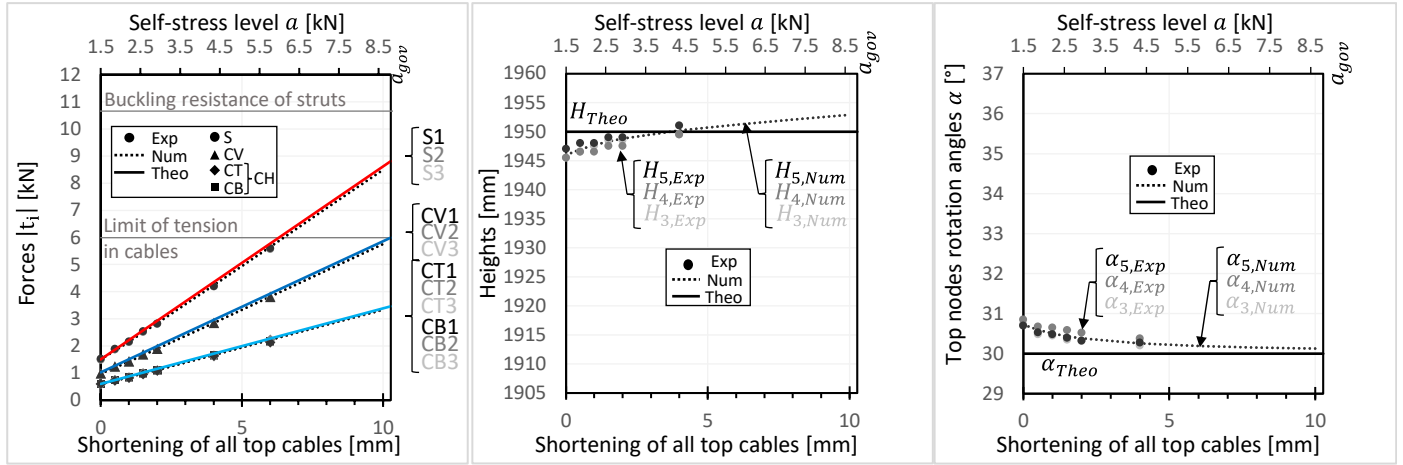
a



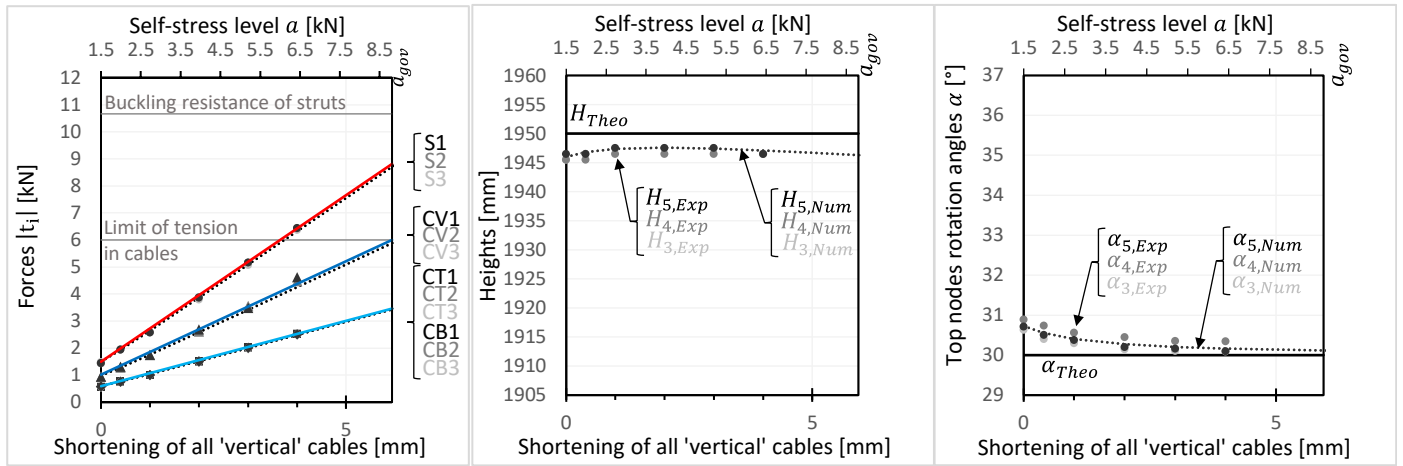
b



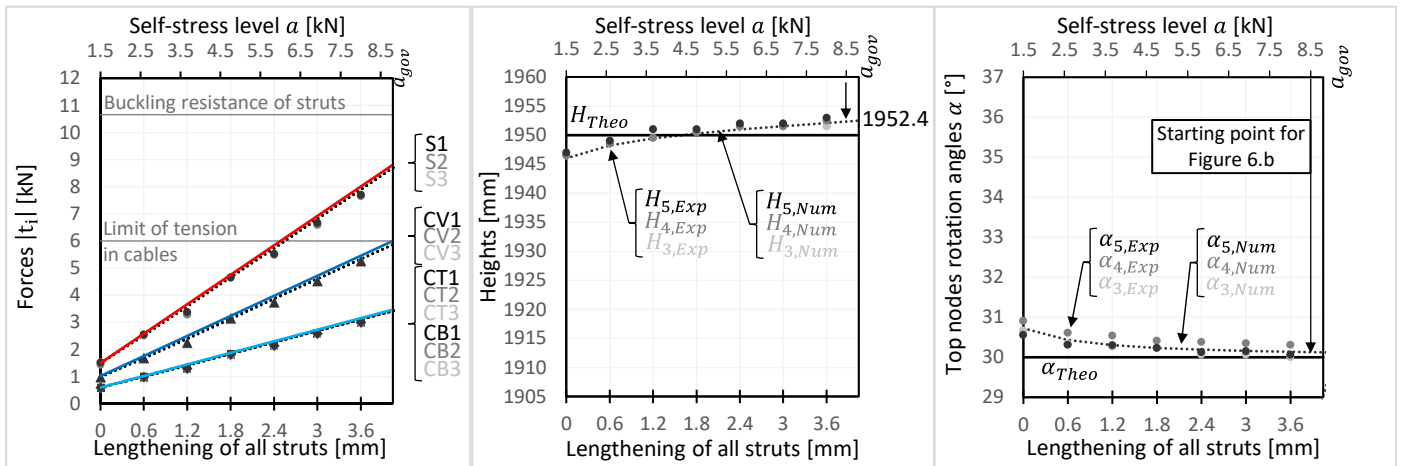
c



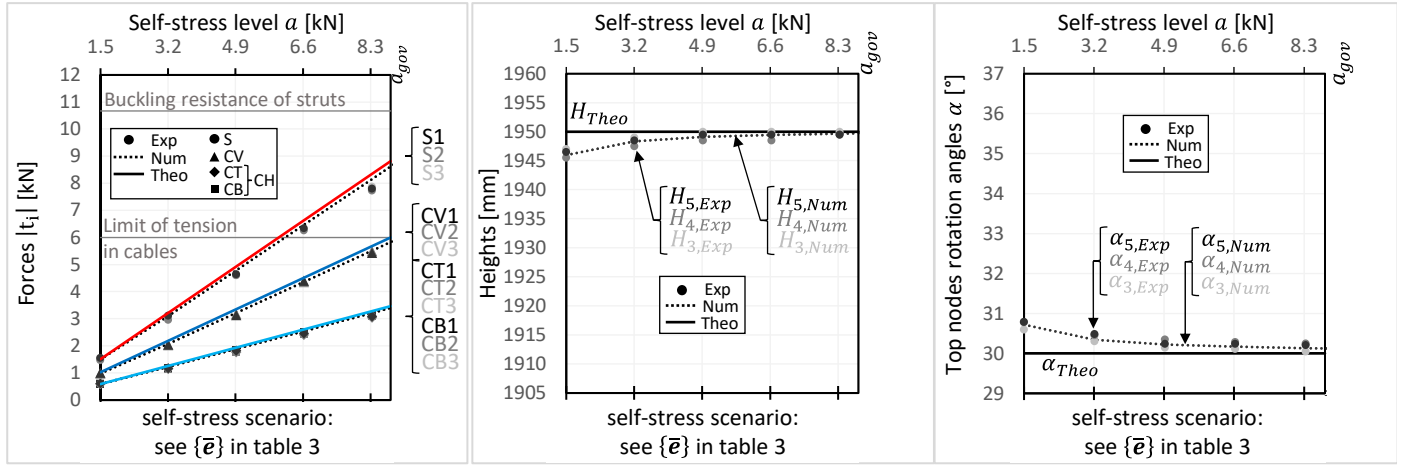
d



e



f



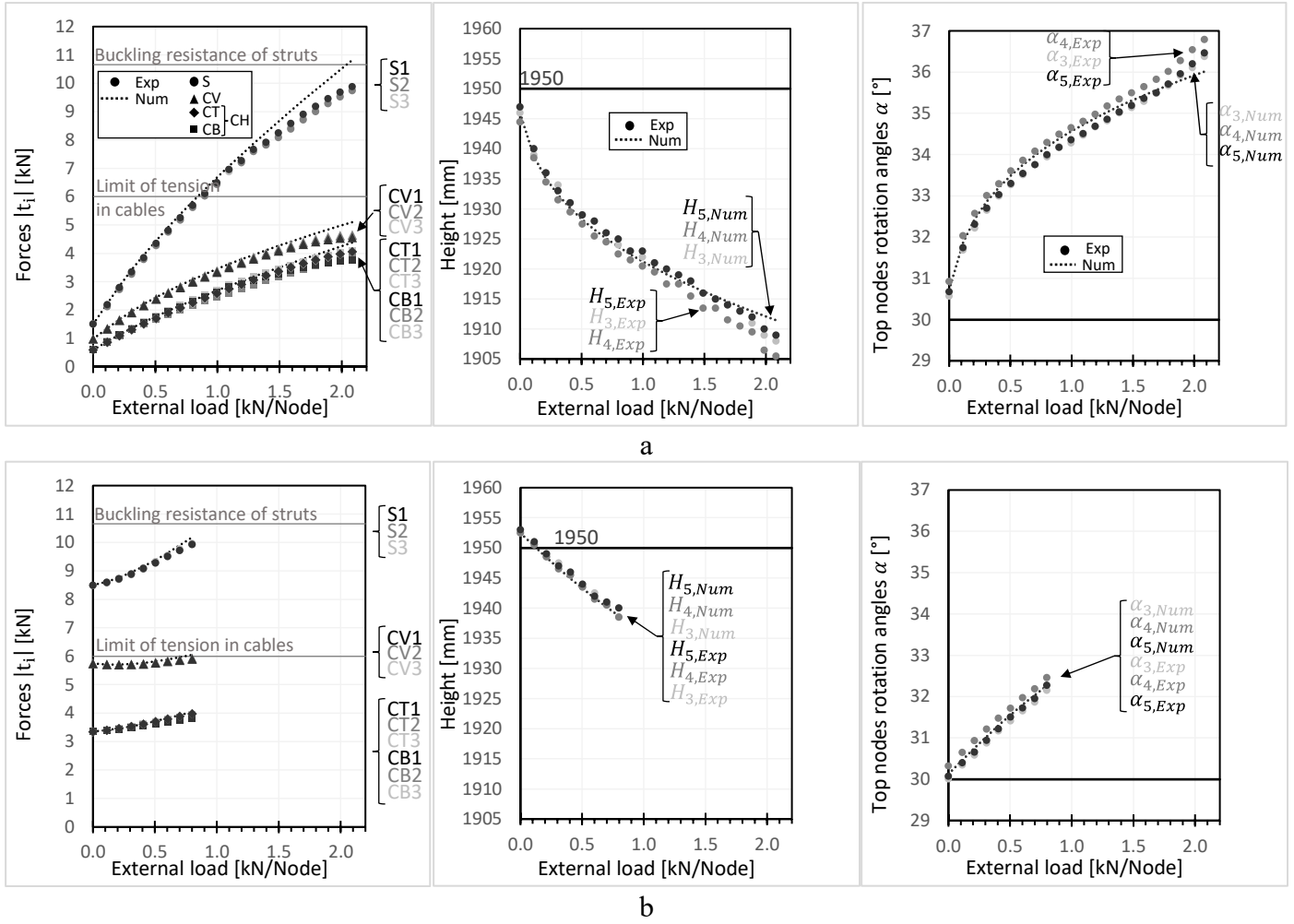
g

Figure 5. Effect of prestressing a) one horizontal top cable, b) one vertical cable, c) one strut, d) all three horizontal top cables, e) all three vertical cables, f) all three struts and g) all cables and struts (self-stress scenario) in internal forces, height and angles of rotation of the simplex model.

Figure 6 shows the effect of compressive vertical loading on the simplex model starting from two different self-stress levels. The internal forces (first column) and the geometry as described by the height and rotation angles (columns two and three) were monitored and are compared with the numerical calculations only. In both cases, the forces in the model as well as the height and angle of rotation show a nonlinear correlation with the load applied. Increasing the load applied on the model increases the internal forces in its elements, decreases its height and increases the angles of rotation. The effects measured are in agreement with the numerical results obtained using dynamic relaxation. However, as the load increases, differences between experimental and numerical results appear with more important differences for the first loading test. In the first test (Figure 6.a), for loads higher than 1.3kN per top node (corresponding to a geometry with  $H=1919$  mm and  $\alpha=35.0^\circ$ ), the measured forces are lower than the numerically calculated ones while the measured displacements are higher than the calculated ones. Under the maximum load applied (2.1 kN per top node), the measured compressive forces in the struts S1, S2, and S3 are -9.88, -9.73, and -9.75 kN, respectively, whereas the numerically predicted value for all struts is of -10.80 kN. These differences may be explained by a bending of the struts in the physical model as the geometry is highly distorted ( $\alpha \geq 35.0^\circ$  see

460 details in discussion). Pictures of the final loading stage for both experiments are available in Appendix B in  
 461 (Feron et al., 2022).

462



463 Figure 6. Effect of vertical loads suspended on the top nodes starting from a) self-stress level  $\alpha = 1.5\text{kN}$  and b) self-stress level  $\alpha = 8.5\text{kN}$ .

464

465

## 466 DISCUSSION

### 467 Mechanism activation due to compressive loading

468 Figure 7 combines the results of Figure 6 (numerical loading) and Figure 4 (theoretical mechanism).  
469 Figure 7.a shows that, no matter the initial self-stress level  $\alpha$ , the numerical displacements (computed by  
470 dynamic relaxation) due to the compressive vertical loading of the simplex follow the same linear trend with  
471 the theoretical mechanism as expressed by the relation between height  $H$  and the rotation angle  $\alpha$ . Starting  
472 from a self-stress level  $\alpha = 1.5\text{kN}$  (Figure 6.a) the compressive load follows the path of the theoretical  
473 mechanism from angles  $\alpha = 30.7^\circ$  to  $36.0^\circ$ . At self-stress level  $\alpha = 1.5\text{kN}$ , the self-weight (41.6N/top node)  
474 is responsible for the mechanism activation from angles  $\alpha = 30.0^\circ$  to  $30.7^\circ$  (justifying the gap before  $\alpha =$   
475  $30.7^\circ$  in Figure 7.a). When starting from the self-stress level  $\alpha = 8.5\text{kN}$  (Figure 6.b) however, the loading  
476 curve in Figure 7.a is always 2.4mm higher than the theoretical mechanism. This is explained by the fact the  
477 8.5kN self-stress level is implemented by 3.95mm lengthening of all struts (see the prestressed geometry in  
478 Figure 5.f). At self-stress level  $\alpha = 8.5\text{kN}$ , the self-weight influence on the mechanism activation is negligible  
479 ( $\alpha = 30.1^\circ$  without other external loads). Moreover, Figure 7 shows that the deformed geometry under this  
480 compressive load can be defined by a single scalar  $\beta$  that characterizes the mechanism activation (Figure 7.b).  
481 The elastic deformation of the simplex under this axial compressive loading is, in this case, negligible  
482 compared to the twisting effect induced by the mechanism activation (Figure 4). Extensional displacements  
483 are thus assumed negligible with the scalar  $\beta$  defining the displacements  $\{\mathbf{d}\} = \{\mathbf{U}^m\}\beta$  induced by the  
484 external loads  $\{\mathbf{f}\}$ .

485 Figure 7.b shows that the relationship between the applied compressive loads and the scalar  $\beta$ . The  
486 relationship is found to depend on the initial self-stress level  $\alpha$ , and takes a scalar to scalar form. This suggests  
487 that the relationship could take the form  $f^m = K^T \beta$  where  $K^T$  is a non constant stiffness scalar that depends  
488 on the self-stress level  $\alpha$ , and  $f^m$  is a scalar that represent the excitation of the mechanism by the loads such

that  $f^m = \{\mathbf{U}^m\}^T \{\mathbf{f}\}$  is obtained by orthogonal projection of the loads  $\{\mathbf{f}\}$  on the inextensional mode  $\{\mathbf{U}^m\}$ . It was indeed verified through dynamic relaxation that different load cases  $\{\mathbf{f}\}$  (e.g. 3kN hanged on one top node or 1kN hanged on three top nodes, or 0.91kN applied in the X direction on node 3,...) having the same value of  $f^m$  (e.g.  $\{\mathbf{U}^m\}^T \{\mathbf{f}\} = 3 \text{ kN}$ ) lead to the same deformed geometry  $\beta$  (assuming negligible extensional displacements) but different internal forces.

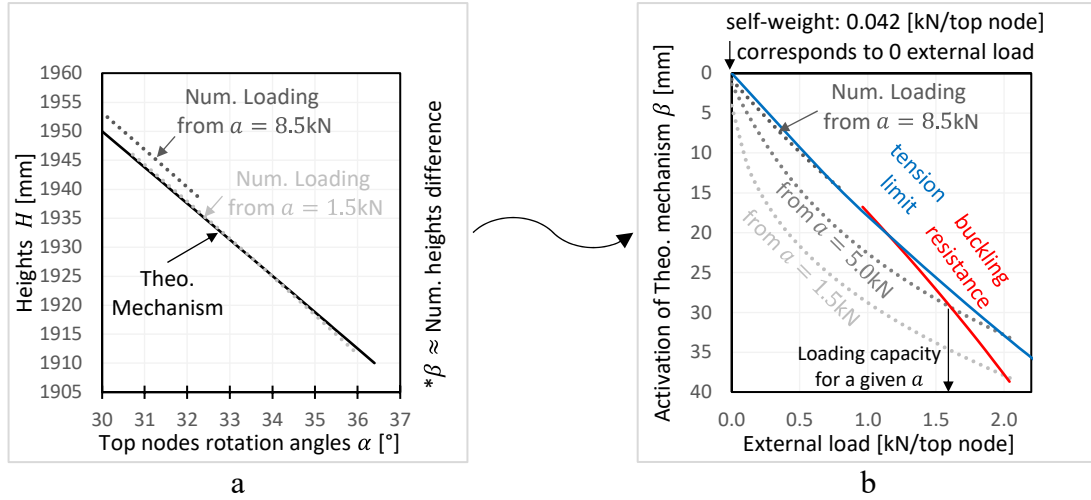


Figure 7. Comparison of numerical displacements and theoretical “infinitesimal” mechanism. a: Due to the linear trends between angles  $\alpha$  and heights  $H$ , b: there exist scalar non-linear functions between external load and the coefficient  $\beta$  of mechanism activation.

Because the self-weight could be included in the external compressive loads (even though this is not considered in this paper), Figure 7.b suggests that the theoretical assumption  $\beta = 0\text{mm}$  during the prestressing phase (see Background chapter) may be correct only if the self-weight is truly null (i.e. in outer space) or at least if it is negligible compared to the self-stress level  $a$ .

Eventually, Figure 7.b provides the compressive loading capacity of the simplex model which depends on the initial self-stress level  $a$ . The loading capacity can be governed either by the struts buckling resistance (-10.66kN) for lightly prestressed simplex, either by the (6kN) limit of tension in vertical cables for heavily prestressed simplex. Remind that the self-stress level  $a = 8.81\text{kN}$  has a null loading capacity (Figure 3) and that Figure 7.b loading capacity is only valid for the vertical loading of the three top nodes (not the other load cases with the same scalars  $f^m$  and  $\beta$ ).



## 506 Starting self-stress level

507 All tests with the exception of the second loading test started from the initial state shown in Figure 2.b  
 508 (assumed equal to the theoretical self-stress level  $\alpha = 1.5\text{kN}$  without considering self-weight in Figure 2.a).  
 509 This self-stress state was defined by the minimal tension of  $0.59\text{kN}$  required by cables to eliminate the bending  
 510 effect of self-weight (see Appendix C in (Feron et al., 2022)), and was implemented by a  $0.75\text{mm}$  lengthening  
 511 of the struts (Figure 2.b and Figure 8). A theoretical zero self-stress can be obtained through form-finding (see  
 512 Appendix A in (Feron et al., 2022)), but in the physical model, the zero self-stress do not exist because of the  
 513 self-weight. Therefore, a “zero-self-stress level” can only be achieved by tuning the struts lengths after the  
 514 assembly of the structure until the forces measured in the struts reflect the effect of self-weight only (see  
 515  $0.66\text{kN}$  in Figure 8). Figure 8 shows that when starting from this “zero-self-stress level”, the increase in  
 516 internal forces is initially nonlinear in relation with the imposed elongation in the struts. It is only after a  
 517 certain threshold that the forces converge towards the linear behavior observed in Figure 5. Therefore, the  
 518 linear sensitivity matrix  $[SM^a]$  analysis provides good estimates only if a minimum self-stress is applied to  
 519 the structure.

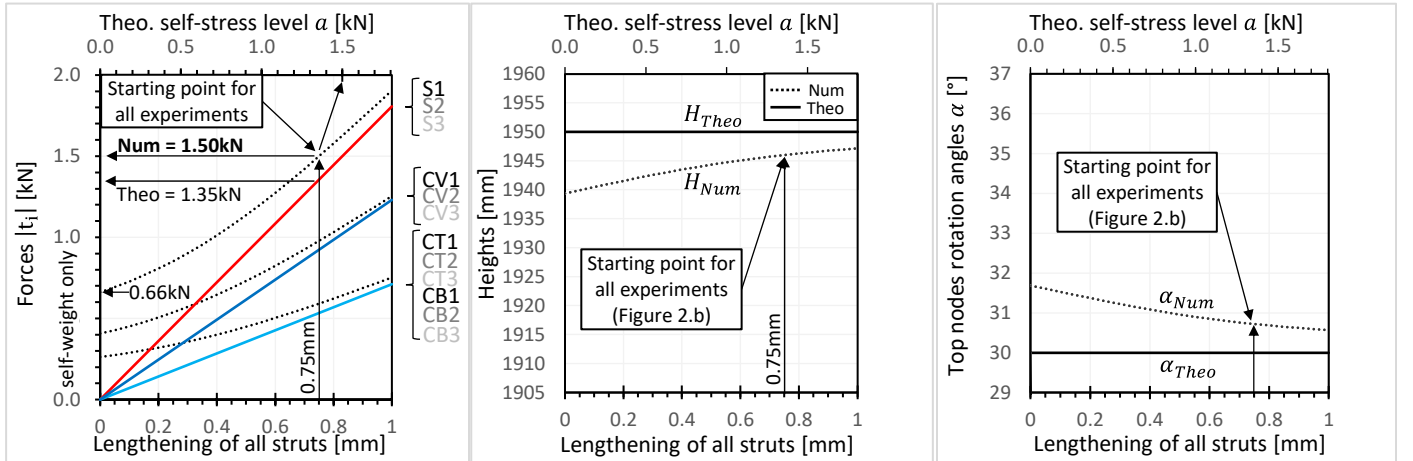


Figure 8. Theoretical and numerical results starting from a state with zero self-stress forces (self-weight only).

## 522 Choice of a prestress scenario and self-stress mode stiffness

523 One can observe that in all prestressing tests starting from the self-stress level  $a = 1.5\text{kN}$ , the forces  
 524 increase is linear in relation with the imposed length variations. The sensitivity matrix  $[SM^a]$  provides thus  
 525 good estimates of the required elongation (Table 4).

526 *Table 4. Imposed elongations for an increase in self-stress level from  $a = 1.5\text{kN}$  to  $a_{gov} = 8.81\text{kN}$  according to the sensitivity matrix  $[SM^a]$ .*

Number of elements prestressed	Elongation in top cable(s)	Elongation in vertical cable(s)	Elongation in strut(s)
1	-30.8mm	-17.8mm	+12.1mm
3	-10.3mm	- 5.9mm	+ 4.0mm

527  
 528 Following the results of the sensitivity matrix  $[SM^a]$  in Table 4, it is clear that shortening three top  
 529 cables (-10.3mm in Table 4) requires three times less length variation per element than shortening only one  
 530 top cable (-30.8mm in Table 4), i.e.  $-30.8 = 3 \cdot -10.3$ . The similar trend is found for other element groups  
 531 (three vertical cables compared with one vertical cable or three struts compared with one strut) with  
 532 differences only due to rounding errors. However, it is observed that when comparing different element groups  
 533 (e.g. -30.8mm shortening in one top cable compared with +12.1mm elongation in one strut), the length  
 534 variation can be expressed as a function of the self-stress mode (e.g. coefficient 0.393 for the top cable and -  
 535 1.000 for the strut in Table 2), i.e.  $-30.8 \cdot 0.393 = +12.1 \cdot -1.000$ . Therefore, the length(s) variation required  
 536 to increase the self-stress level is not directly related to the stiffness  $K_{ii}^e$  of the element  $i$  being activated but it  
 537 depends on the self-stress mode  $[S]$  and the stiffness of the self-stress mode itself. A self-stress mode stiffness  
 538  $[K^S]$  can thus be defined using equation ( 7 ):

$$\{\mathbf{a}\} = \underbrace{-\frac{[SM^a]}{([S]^T[K^e]^{-1}[S])^{-1}}[S]^T}_{[K^S]} \{\bar{\mathbf{e}}\} \quad (16)$$

539

Where the matrix  $[K^S]$  has  $s$  rows and columns. Since the simplex has only  $s = 1$  self-stress mode, its scalar stiffness is given by  $K^S = 602\text{N/mm}$ . Values of  $[SM^a]$  in Table 2 are thus simply obtained given the self-stress mode stiffness  $K^S$  and equation ( 16 ).

Hence, if wondering which elements shall be activated to increase the self-stress level, it might be advantageous to use the ones having the higher coefficient in the self-stress mode (in the case of the simplex model, it is the struts) because they will require less elongation and distort less the geometry of the structure. For instance, the +12.1mm lengthening of one strut (Figure 5.c) distorts less the geometry than the -17.8mm shortening of one vertical cable (Figure 5.b) because their coefficients in the self-stress mode are respectively -1.000 and 0.681 (Table 2).

### Limitations of the used theoretical approach

Theoretical developments included in this study assumed no change in the geometry i.e. no change in the equilibrium matrix and self-stress mode, and a null activation of the simplex mechanism.

After computing the geometric stiffness matrix  $[K^G]$  from the internal forces in the initial self-stress state (Figure 2.a), one can observe that for this simplex model the two forms  $[SM^{d2}]$  and  $[SM^{d3}]$  are almost identical (Feron et al., 2022). Figure 9 shows the displacements calculated with  $[SM^{d2}]$  for the shortening of the top cable CT3 by -30.8mm. Calculations using  $[SM^{d2}]$  are found to be in agreement with the results obtained using dynamic relaxation when the self-stress level is sufficient high to avoid the mechanism activation due to self-weight. However, when the self-stress level is low, theoretical and experimental diverge. Theoretical results can be corrected by either considering the activation of the mechanism through the coefficient  $\beta$  (Figure 4) or by recomputing the equilibrium matrix using iterative methods (Saeed, 2022; Xu & Luo, 2009; Yuan et al., 2016; P. Zhang et al., 2014). Figure 9 highlights thus also the nonlinear behavior of the structure which is not considered in the used theoretical approach with its effect being greater for low self-stress level.

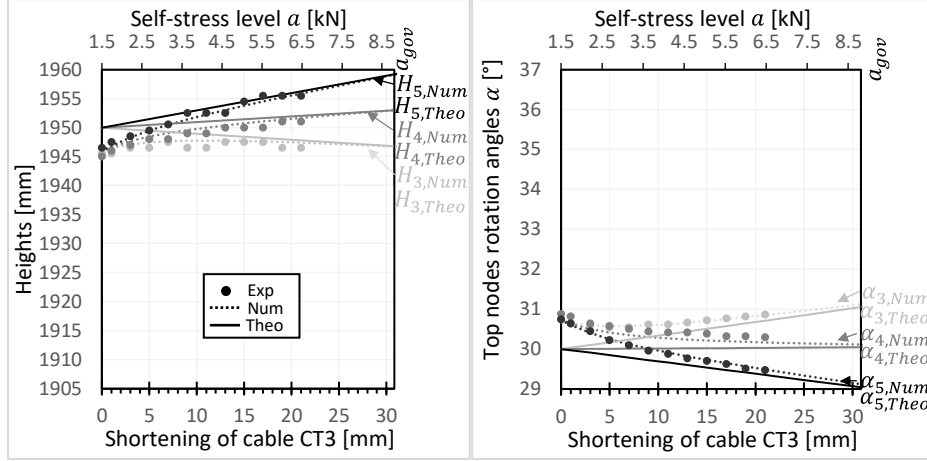
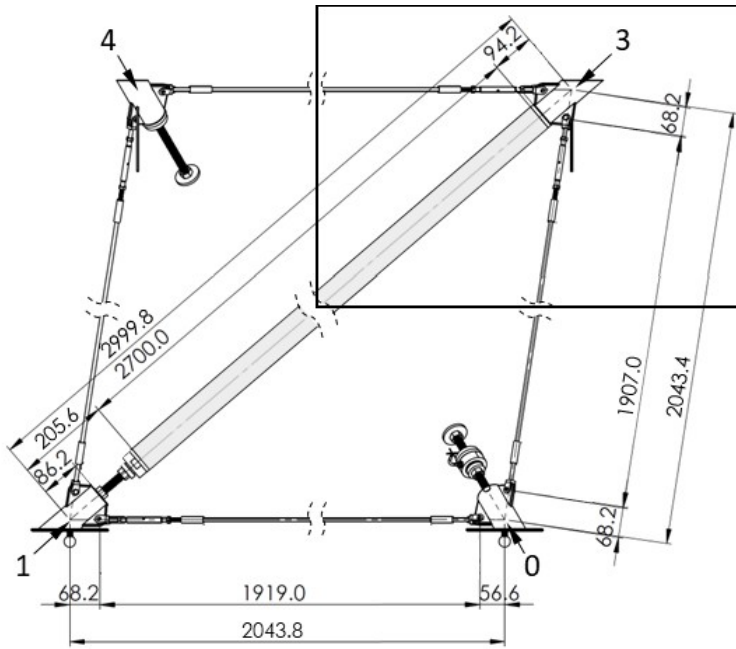


Figure 9. Comparison of the displacements obtained using the displacement sensitivity matrix  $[SM^{d2}]$  and dynamic relaxation.

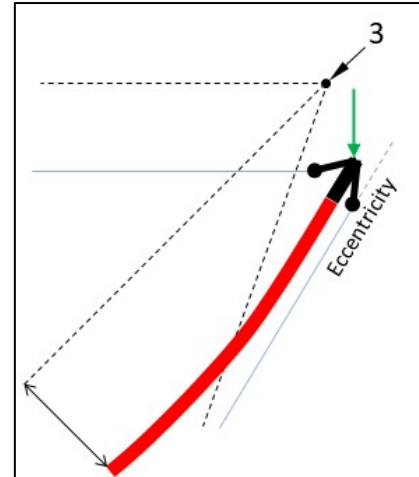
## Joints influence and limitation of the used numerical approach

Numerical results obtained using dynamic relaxation show good correlation with the experimental results (Figure 5 and Figure 6.b) with the exception of the case of the compressive loading starting from a low self-stress level (Figure 6.a) due to parasite moments.

Nodal displacements (in terms of angles of rotation) are more important in the loading test starting from low self-stress ( $\alpha_{num} = 36.0^\circ$  in Figure 6.a) than from high self-stress ( $\alpha_{num} = 32.3^\circ$  in Figure 6.b) compared to the initial theoretical geometry ( $\alpha_{theo} = 30.0^\circ$ ) in which the joints were designed (Figure 10.a). Because joints are perfectly pin-jointed only when  $\alpha_{exp} = 30.0^\circ$  (all element axes being concurrent to a point in the joint), when large displacements occur and the geometry is distorted parasitic bending moments occur in the joints (see the axial forces eccentricities with the node in Figure 10.b). It is thus concluded that large displacements induce bending moments in the physical model that are responsible for the numerical to experimental lack of agreement in Figure 6.a. Improvements in joint design and modeling should thus be considered for better agreement. Note that geometric imperfections (e.g. initial struts curvature, etc) may be inevitable in larger scale model (Cai et al., 2019; Coughlin & Stamenović, 1997).



a



b

Figure 10. Joints influence. a: Front view of the initial geometry with dimensions in [mm]; b: Schematic illustration of the deformed geometry

## 582 CONCLUSION

583 Self-stress is critical for tensegrity structures as it defines their existence by defining their stability and  
584 behavior under loading. This study thus focused on the self-stress implementation considering different  
585 *prestress scenarios* (i.e. combination of imposed elongations through mechanical devices), and the static  
586 loading through the testing of human-scale physical simplex model. The behavior of the model was assessed  
587 through the measurement of all element forces combined with measurements of the simplex geometry (height  
588 and angle of rotation of each top node with respect to its bottom node). Experimental results were compared  
589 with theoretical and numerical results obtained through linear analyses on the basis of the equilibrium matrix  
590 and using the dynamic relaxation method.

591 At prestressing stage implemented via imposed elongations with mechanical devices in all elements,  
592 the study shows that results obtained with the dynamic relaxation method correlate well with the measured  
593 forces and changes in geometry. Regarding the theoretical-experimental comparison, it is shown that, in terms  
594 of forces, prestressing any element or combination of elements will lead to the implementation of a single  
595 self-stress mode with internal forces in the model following the same linear trend. This linear force increase  
596 is captured well by the self-stress level sensitivity matrix  $[SM^a]$  except when the self-stress level is smaller  
597 than 1.5kN (=17% of the maximum allowed level  $a_{gov} = 8.8\text{kN}$ ). Attention has thus to be given when the  
598 self-stress is low as self-weight can affect both the force distribution and the geometry of prestressed  
599 mechanism. In terms of geometry, it is shown that the imposed elongations are responsible for displacements  
600 compared to the targeted theoretical nodes positions except if a *self-stress scenario* is implemented (i.e.  
601 lengthening of all struts and shortening of all cables by certain precise values provided in this article). Other  
602 choices of prestress scenarios altering the lengths of only three elements can lead to symmetric geometry with  
603 small deviations compared to the target. In case of high self-stress level, rotation angles are close to  $30^\circ$  and  
604 the top base is flat but with nodes heights varying from -3.8mm (three vertical cables shortening) to +3.1mm

(three top cables shortening) compared to 1950mm theoretical height. In case of low self-stress level, self-weight may be regarded as a compressive load activating the simplex mechanism with the scalar  $\beta$  that may be considered different than 0mm in the theoretical approach. Increase of the self-stress level has a non-linear effect on the infinitesimal mechanism activation  $\beta$ . Another way to consider this non-linear effect may be the use of recent iterative procedures where the equilibrium matrix, the self-stress mode and the sensitivity matrices are recomputed at each step. Eventually, a targeted self-stress level can always be obtained by actuating one element only but in these cases the geometry can be significantly distorted (rotation angles from 29 to 31° for 30.8mm shortening of one top cable or uneven top base with 23.4mm height difference for 17.8mm shortening of one vertical cable). The concept of self-stress mode stiffness is introduced to provide a linear estimation of the length variations required to implement a certain self-stress level in function of the chosen prestress scenario.

Self-stress also impacts the behavior under loading which is found to be nonlinear with respect to the compressive load applied on the structure. The load bearing capacity is of course less for highly prestressed systems. Deformed geometry was found to follow the simplex inextensional displacements  $\{\mathbf{d}\} = \{\mathbf{U}^m\}\beta$  whatever the self-stress level and the amount of vertical loads. The scalar  $\beta$  describes thus entirely the deformed geometry of the simplex when extensional displacements are negligible compared to the mechanism activation. Similarly, a scalar formulation of any load  $\{\mathbf{f}\}$  was proposed by orthogonal projection  $f^m = \{\mathbf{U}^m\}^T \{\mathbf{f}\}$ . The scalar  $f^m$  describes thus the participation of any load  $\{\mathbf{f}\}$  in the excitation of the mechanism  $\{\mathbf{U}^m\}$ . For a certain equivalent load  $f^m$ , whatever the load case  $\{\mathbf{f}\}$ , it is shown that the deformed geometry  $\beta$  is uniquely defined with  $\beta$  being defined such that  $f^m = K^T \beta$  where  $K^T$  is a non-linear tangent stiffness scalar depending on the initial self-stress level. Equilibrium of forces can thus be approximated in the deformed geometry  $\beta$  when extensional displacements are negligible.

627 All experimental measurements are open-accessible for interested readers willing to address the  
628 presented limitations.

## 629 **FUNDING**

630 Project subsidized by Brussels Capital Region – Innoviris.

## 631 **DATA AVAILABILITY STATEMENT**

632 Data, models, or code generated or used during the study are available in a repository online (Feron et  
633 al., 2022) in accordance with funder data retention policies.

## 634 **ACKNOWLEDGEMENT**

635 The authors would like to thank:

- 636 - BESIX, for their support in particular chief modeler Carlos Esteves for design advices as well as  
637 senior project manager Pierre Mengeot and president of innovation board Thomas Vandenberg  
638 for supervision;
- 639 - The LEMSC, in particular director Catherine Doneux, electronic instruments expert Alex  
640 Bertholet, data acquisition expert Antoine Bietlot, testing platform supervisor Christophe Bayart,  
641 specialized technicians Quentin Mestrez and Vincent Forzee as well as all team members for their  
642 excellence and illimited support;
- 643 - Malcourant Mécanique, for the professional procurement, fabrication and welding of the different  
644 parts and material and in particular to senior design manager Patrick Powis;
- 645 - Master thesis students Romain Antoine and Nicolas Danzin for their collaboration;
- 646 - Sébastien François and Sébastien Lambot for the loan of the theodolite for many months;
- 647 - The three anonymous reviewers for constructive advice leading to the improvement of this article.



## REFERENCES

- Aloui, O., Flores, J., Orden, D., & Rhode-Barbarigos, L. (2019). Cellular morphogenesis of three-dimensional tensegrity structures. *Computer Methods in Applied Mechanics and Engineering*, 346, 85–108. <https://doi.org/10.1016/j.cma.2018.10.048>
- Aloui, O., Orden, D., & Rhode-Barbarigos, L. (2018a). Generation of planar tensegrity structures through cellular multiplication. *Applied Mathematical Modelling*, 64, 71–92. <https://doi.org/10.1016/j.apm.2018.07.024>
- Aloui, O., Flores, J., & Rhode-Barbarigos, L. (2018b). Re-discovering the Tensegrity Simplex: decomposition, self-stress analysis and alternative designs. *IASS 2018 Boston Symposium: Kenneth Snelson Memorial*. <https://www.ingentaconnect.com/contentone/iass/piass/2018/00002018/00000027/art00018>
- Averseng, J., & Crosnier, B. (2004). Prestressing tensegrity systems - application to multiple selfstress state structures. *International Journal of Structural Stability and Dynamics*, 04(04), 543–557. <https://doi.org/10.1142/S0219455404001379>
- Averseng, J., Kazi-Aoual, M. N., & Crosnier, B. (2002). Tensegrity systems selfstress state implementation methodology. *Space Structures* 5, 1: 31-38. <https://doi.org/10.1680/ss5v1.31739.0004>
- Barnes, M. R. (1988). Form-finding and analysis of prestressed nets and membranes. *Computers and Structures*, 30(3), 685–695. [https://doi.org/10.1016/0045-7949\(88\)90304-5](https://doi.org/10.1016/0045-7949(88)90304-5)
- Barnes, M. R. (1999). Form Finding and Analysis of Tension Structures by Dynamic Relaxation. *International Journal of Space Structures*, 14(2), 89–104. <https://doi.org/10.1260/0266351991494722>
- Bel Hadj Ali, N., Rhode-Barbarigos, L., & Smith, I. F. C. (2011). Analysis of clustered tensegrity structures using a modified dynamic relaxation algorithm. *International Journal of Solids and Structures*, 48(5), 637–647. <https://doi.org/10.1016/j.ijsolstr.2010.10.029>
- Belytschko, T. B., & Hugues, T. J. R. (1983). *Computational Methods for Transient Analysis*. Computational Methods in Mechanics.
- Cai, J., Yang, R., Wang, X., & Feng, J. (2019). Effect of initial imperfections of struts on the mechanical behavior of tensegrity structures. *Composite Structures*, 207, 871–876. <https://doi.org/10.1016/j.compstruct.2018.09.018>
- Calladine, C. R. (1978). Buckminster Fuller's "Tensegrity" structures and Clerk Maxwell's rules for the construction of stiff frames. *International Journal of Solids and Structures*, 14(2), 161–172. [https://doi.org/10.1016/0020-7683\(78\)90052-5](https://doi.org/10.1016/0020-7683(78)90052-5)
- Calladine, C. R., & Pellegrino, S. (1991). First-order infinitesimal mechanisms. *International Journal of Solids and Structures*, 27(4), 505–515. [https://doi.org/10.1016/0020-7683\(91\)90137-5](https://doi.org/10.1016/0020-7683(91)90137-5)
- CEN. (2009). *EN 1999-1-1:2007+AI:2009 - Eurocode 9 - Design of aluminium structures - Part 1-1: General structural rules*.
- Chen, L., Jiang, Z., Gao, W., & Zhou, Y. (2020). Identification and Adjustment of the Pretension Deviation in Cable-Strut Tensile Structures. *KSCE Journal of Civil Engineering*, 24(1), 143–152. <https://doi.org/10.1007/s12205-020-1473-4>
- Chen, L., Deng, H., Cui, Y., Dong, S., & Zhou, Y. (2016). Theoretical analysis and experimental study on sensitivity of element-length error in cable-strut tensile structures. *Advances in Structural Engineering*, 19(9), 1463–1471. <https://doi.org/10.1177/1369433216643245>
- Connelly, R. (2002). Tensegrity structures: why are they stable? In *Rigidity theory and applications* (pp. 47–54). Springer.
- Coughlin, M. F., & Stamenović, D. (1997). A tensegrity structure with buckling compression elements: Application to cell mechanics. *Journal of Applied Mechanics*, 64(3), 480–486. <https://doi.org/10.1115/1.2788918>

684 Cundall, P. (1976). Explicit finite-difference methods in geomechanics. *Second Int. Conf. Numerical Methods in Geomechanics*,  
685 Blacksburg, 132–150.

686 Day, A. S. (1965). An introduction to dynamic relaxation. *The Engineer*, 219, 218–221.

687 Deng, H., & Kwan, A. S. K. (2005). Unified classification of stability of pin-jointed bar assemblies. *International Journal of Solids*  
688 *and Structures*, 42(15), 4393–4413. <https://doi.org/10.1016/J.IJSOLSTR.2005.01.009>

689 Dubé, J. F., Angellier, N., & Crosnier, B. (2008). Comparison between experimental tests and numerical simulations carried out on  
690 a tensegrity minigrid. *Engineering Structures*, 30(7), 1905–1912. <https://doi.org/10.1016/j.engstruct.2007.12.010>

691 Estrada, G. G., Bungartz, H. J., & Mohrdieck, C. (2006). Numerical form-finding of tensegrity structures. *International Journal of*  
692 *Solids and Structures*, 43(22–23), 6855–6868. <https://doi.org/10.1016/j.ijsolstr.2006.02.012>

693 Faroughi, S., & Lee, J. (2014). Geometrical nonlinear analysis of tensegrity based on a co-rotational method. *Advances in Structural*  
694 *Engineering*, 17(1), 41–51. <https://doi.org/10.1260/1369-4332.17.1.41>

695 Feron, J., Bertholet, A., & Latteur, P. (2022). *Replication Data for: Experimental testing of a tensegrity simplex: self-stress*  
696 *implementation and static loading*. Open Data @ UCLouvain. <https://doi.org/10.14428/DVN/CDLVFV>

697 Feron, J., Boucher, L., Denoël, V., & Latteur, P. (2019). Optimization of Footbridges Composed of Prismatic Tensegrity Modules.  
698 *ASCE Journal of Bridge Engineering*, 24(12). [https://doi.org/10.1061/\(ASCE\)BE.1943-5592.0001438](https://doi.org/10.1061/(ASCE)BE.1943-5592.0001438).

699 Feron, J., Mengeot, P., Vandenbergh, T., & Latteur, P. (2021). A deployable tensegrity footbridge: static design and optimization.  
700 *IABSE Congress, Ghent 2021: Structural Engineering for Future Societal Needs*, 1196–1204.  
701 <https://doi.org/10.2749/GHENT.2021.1196>

702 Fraternali, F., Carpentieri, G., & Amendola, A. (2015). On the mechanical modeling of the extreme softening/stiffening response  
703 of axially loaded tensegrity prisms. *Journal of the Mechanics and Physics of Solids*, 74, 136–157.  
704 <https://doi.org/10.1016/j.jmps.2014.10.010>

705 Guest, S. D. (2011). The stiffness of tensegrity structures. *IMA Journal of Applied Mathematics*, 76(1), 57–66.  
706 <https://doi.org/10.1093/imamat/hxq065>

707 Hanaor, A. (2012). Debunking “Tensegrity” - A Personal Perspective. *International Journal of Space Structures*, 27(2), 179–183.  
708 <https://doi.org/10.1260/0266-3511.27.2-3.179>

709 Hrazmi, I., Averseng, J., Quirant, J., & Jamin, F. (2021). Deployable double layer tensegrity grid platforms for sea accessibility.  
710 *Engineering Structures*, 231, 111706. <https://doi.org/10.1016/j.engstruct.2020.111706>

711 Jauregui, V. G. (2010). *Tensegrity structures and their application to architecture*. Publican.

712 Juan, S. H., & Mirats Tur, J. M. (2008). Tensegrity frameworks: Static analysis review. *Mechanism and Machine Theory*, 43(7),  
713 859–881. <https://doi.org/10.1016/j.mechmachtheory.2007.06.010>

714 Kawaguchi, K., Hangai, Y., Pellegrino, S., & Furuya, H. (1996). Shape and Stress Control Analysis of Prestressed Truss Structures:  
715 *Journal of Reinforced Plastics and Composites*, 15(12), 1226–1236. <https://doi.org/10.1177/073168449601501204>

716 Kawaguchi, K., & Lu, Z.-Y. (2002). Construction of three-strut tension systems. *Space Structures* 5, 1: 1-10.  
717 <https://doi.org/10.1680/ss5v1.31739.0001>

718 Kawaguchi, K., & Mizutani, K. (2018). Tensegrity Skeletons and Prestressing Process. *IASS 2018 Boston Symposium: Kenneth*  
719 *Snelson Memorial*, 1–5.

720 Kebiche, K., Kazi-Aoual, M. N., & Motro, R. (1999). Geometrical non-linear analysis of tensegrity systems. *Engineering*  
721 *Structures*, 21(9), 864–876. [https://doi.org/10.1016/S0141-0296\(98\)00014-5](https://doi.org/10.1016/S0141-0296(98)00014-5)

722 Klimke, H., & Stephan, S. (2004). The making of a tensegrity tower. *IASS Symposium*.

723 Kwan, A. S. K., & Pellegrino, S. (1993). Prestressing a space structure. *AIAA Journal*, 31(10), 1961–1963.  
724 <https://doi.org/10.2514/3.11876>

725 Leica Geosystem. (n.d.). *Leica TPS1200 Series - High performance Total Station*. Retrieved 5 December 2021, from  
726 <https://secure.fltgeosystems.com/uploads/tips/documents/39.pdf>

727 Luo, B., Sun, Y., Guo, Z. X., & Pan, H. (2016). Multiple random-error effect analysis of cable length and tension of cable-strut  
728 tensile structure. *Advances in Structural Engineering*, 19(8), 1289–1301. <https://doi.org/10.1177/1369433216634534>

729 Ma, S., Chen, M., & Skelton, R. E. (2022). Tensegrity system dynamics based on finite element method. *Composite Structures*,  
730 280. <https://doi.org/10.1016/j.compstruct.2021.114838>

731 Maxwell, J. C. (1864). L. On the calculation of the equilibrium and stiffness of frames. *The London, Edinburgh, and Dublin*  
732 *Philosophical Magazine and Journal of Science*, 27(182), 294–299. <https://doi.org/10.1080/14786446408643668>

733 Micheletti, A. (2012). Modular Tensegrity Structures: The "Tor Vergata" Footbridge. *Mechanics, Models and Methods*, 61, 375–  
734 384. [https://doi.org/10.1007/978-3-642-24638-8\\_25](https://doi.org/10.1007/978-3-642-24638-8_25)

735 Micheletti, A., & Podio-Guidugli, P. (2022). Seventy years of tensegrities (and counting). *Archive of Applied Mechanics*, 92(9),  
736 2525–2548. <https://doi.org/10.1007/s00419-022-02192-4>

737 Motro, R. (2003). *Tensegrity: Structural Systems for the Future* (H. Penton, Ed.).

738 Motro, R., Najari, S., & Jouanna, P. (1987). Static and Dynamic Analysis of Tensegrity Systems. *Lecture Notes in Engineering*,  
739 270–279. [https://doi.org/10.1007/978-3-642-83015-0\\_24](https://doi.org/10.1007/978-3-642-83015-0_24)

740 Murakami, H. (2001). Static and dynamic analyses of tensegrity structures. Part 1. Nonlinear equations of motion. *International*  
741 *Journal of Solids and Structures*, 38(20), 3599–3613. [https://doi.org/10.1016/S0020-7683\(00\)00232-8](https://doi.org/10.1016/S0020-7683(00)00232-8)

742 Obara, P., Kłosowska, J., & Gilewski, W. (2019). Truth and Myths about 2D Tensegrity Trusses. *Applied Sciences*, 9(179).  
743 <https://doi.org/10.3390/app9010179>

744 Oliveira, M. C., & Skelton, R. E. (2009). *Tensegrity Systems*. Springer US. <https://doi.org/10.1007/978-0-387-74242-7>

745 Papadrakakis, M. (1981). A method for the automatic evaluation of the dynamic relaxation parameters. *Computer Methods in*  
746 *Applied Mechanics and Engineering*, 25(1), 35–48. [https://doi.org/10.1016/0045-7825\(81\)90066-9](https://doi.org/10.1016/0045-7825(81)90066-9)

747 Paronesso, A. (2002). The 2002 world cycling center arena aigle, Switzerland. *International IASS Symposium on "Lightweight*  
748 *Structures in Civil Engineering*.

749 Paronesso, A., & Passera, R. (2004). The cloud of Yverdon. *IASS Symposium*, 184–185.

750 Pellegrino, S. (1990). Analysis of prestressed mechanisms. *International Journal of Solids and Structures*, 26(12), 1329–1350.  
751 [https://doi.org/10.1016/0020-7683\(90\)90082-7](https://doi.org/10.1016/0020-7683(90)90082-7)

752 Pellegrino, S. (1993). Structural computations with the singular value decomposition of the equilibrium matrix. *International*  
753 *Journal of Solids and Structures*, 30(21), 3025–3035. [https://doi.org/10.1016/0020-7683\(93\)90210-X](https://doi.org/10.1016/0020-7683(93)90210-X)

754 Pellegrino, S., & Calladine, C. R. (1986). Matrix analysis of statically and kinematically indeterminate frameworks. *International*  
755 *Journal of Solids and Structures*, 22(4), 409–428. [https://doi.org/10.1016/0020-7683\(86\)90014-4](https://doi.org/10.1016/0020-7683(86)90014-4)

Recski, A. (2008). Combinatorial Conditions for the Rigidity of Tensegrity Frameworks. In *Horizons of Combinatorics* (pp. 163–177). Springer Berlin Heidelberg. [https://doi.org/10.1007/978-3-540-77200-2\\_8](https://doi.org/10.1007/978-3-540-77200-2_8)

Rhode-Barbarigos, L., Hadj Ali, N. B., Motro, R., & Smith, I. F. C. (2010). Designing tensegrity modules for pedestrian bridges. *Engineering Structures*, 32(4), 1158–1167. <https://doi.org/10.1016/j.engstruct.2009.12.042>

Roth, J. K., & McCarthy, T. J. (2021). Optimizing compressive load capacity for differing tensegrity geometries. *Computers & Structures*, 249, 106523. <https://doi.org/10.1016/j.compstruc.2021.106523>

Saeed, N. M. (2022). Displacement Control of Nonlinear Pin-Jointed Assemblies Based on Force Method and Optimization. *AIAA Journal*, 60(2), 1024–1031. <https://doi.org/10.2514/1.J060568>

Saeed, N. M., & Kwan, A. S. K. (2016). Simultaneous displacement and internal force prescription in shape control of pin-jointed assemblies. *Journal of Aircraft*, 53(4), 2499–2506. <https://doi.org/10.2514/1.J054811>

Schek, H.-J. (1974). The force density method for form finding and computation of general networks. *Computer Methods in Applied Mechanics and Engineering*, 3(1), 115–134. [https://doi.org/10.1016/0045-7825\(74\)90045-0](https://doi.org/10.1016/0045-7825(74)90045-0)

Schlaich, M. (2004). The messeturm in rostock - A tensegrity tower. *Journal of the International Association for Shell and Spatial Structures*, 45(145), 93–98.

Sensy. (n.d.-a). *Technical drawings: loading washers for compression annular load cells model A5900-A*. Retrieved 8 November 2021, from [https://files.sensy.com/drawings/ID\\_A5900\\_EN.pdf](https://files.sensy.com/drawings/ID_A5900_EN.pdf)

Sensy. (n.d.-b). *Through hole (annular) load cells model 5900-A-10kN-0.25%*. Retrieved 8 November 2021, from [https://www.sensy.com/en/crane-overload-protection/through-hole-annular-load-cells-5900#/36-capacity-10\\_kn/28-accuracy-025\\_](https://www.sensy.com/en/crane-overload-protection/through-hole-annular-load-cells-5900#/36-capacity-10_kn/28-accuracy-025_)

Shekastehband, B., Abedi, K., & Dianat, N. (2013). Experimental and numerical study on the self-stress design of tensegrity systems. *Meccanica*, 48(10), 2367–2389. <https://doi.org/10.1007/s11012-013-9754-3>

Sultan, C. (2014). Tensegrity deployment using infinitesimal mechanisms. *International Journal of Solids and Structures*, 51(21–22), 3653–3668. <https://doi.org/10.1016/j.ijsolstr.2014.06.025>

Tibert, A. G., & Pellegrino, S. (2003). Review of Form-Finding Methods for Tensegrity Structures. *International Journal of Space Structures*, 18(4), 209–223. <https://doi.org/10.1260/026635103322987940>

Vassart, N., & Motro, R. (1999). Multiparametered Formfinding Method: Application to Tensegrity Systems. *International Journal of Space Structures*, 14(2), 147–154. <https://doi.org/10.1260/0266351991494768>

Veenendaal, D., & Block, P. (2012). An overview and comparison of structural form finding methods for general networks. *International Journal of Solids and Structures*, 49(26), 3741–3753. <https://doi.org/10.1016/j.ijsolstr.2012.08.008>

Wang, Y., Xu, X., & Luo, Y. (2021). A unifying framework for form-finding and topology-finding of tensegrity structures. *Computers & Structures*, 247, 106486. <https://doi.org/10.1016/j.compstruc.2021.106486>

Xu, X., & Luo, Y. (2009). Non-linear displacement control of prestressed cable structures. *Proceedings of the Institution of Mechanical Engineers, Part G: Journal of Aerospace Engineering*, 223(7), 1001–1007. <https://doi.org/10.1243/09544100JAERO455>

Xue, Y., Wang, Y., Xu, X., Wan, H.-P., Luo, Y., & Shen, Y. (2021). Comparison of different sensitivity matrices relating element elongations to structural response of pin-jointed structures. *Mechanics Research Communications*, 118(May), 103789. <https://doi.org/10.1016/j.mechrescom.2021.103789>

793 You, Z. (1997). Displacement control of prestressed structures. *Computer Methods in Applied Mechanics and Engineering*, 144(1–  
794 2), 51–59. [https://doi.org/10.1016/S0045-7825\(96\)01164-4](https://doi.org/10.1016/S0045-7825(96)01164-4)

795 Yuan, X., Liang, X., & Li, A. (2016). Shape and force control of prestressed cable-strut structures based on nonlinear force method.  
796 *Advances in Structural Engineering*, 19(12), 1917–1926. <https://doi.org/10.1177/1369433216652411>

797 Zhang, J. Y., & Ohsaki, M. (2007). Stability conditions for tensegrity structures. *International Journal of Solids and Structures*,  
798 44(11–12), 3875–3886. <https://doi.org/10.1016/j.ijsolstr.2006.10.027>

799 Zhang, P., Kawaguchi, K., & Feng, J. (2014). Prismatic tensegrity structures with additional cables: Integral symmetric states of  
800 self-stress and cable-controlled reconfiguration procedure. *International Journal of Solids and Structures*, 51(25–26),  
801 4294–4306. <https://doi.org/10.1016/j.ijsolstr.2014.08.014>

802 Zhang, P., Xiong, H., & Chen, J. (2020). Unified Fundamental Formulas for Static Analysis of Pin-Jointed Bar Assemblies.  
803 *Symmetry*, 12(6), 994. <https://doi.org/10.3390/sym12060994>  
804  
805